UNCONDITIONALLY ENERGY STABLE TIME STEPPING SCHEME FOR CAHN-MORRAL EQUATION: APPLICATION TO MULTI-COMPONENT SPINODAL DECOMPOSITION AND OPTIMAL SPACE TILING

R. TAVAKOLI

Abstract. An unconditionally energy stable time stepping scheme is introduced to solve Cahn-Morral-like equations in the present study. It is constructed based on the combination of David Eyre's time stepping scheme and Schur complement approach. Although the presented method is general and independent to the choice of homogeneous free energy density function term, logarithmic and polynomial energy functions are specifically considered in this paper. The method is applied to study the spinodal decomposition in multi component systems and optimal space tiling problems. A penalization strategy is developed, in the case of later problem, to avoid trivial solutions. Extensive numerical experiments demonstrate the success and performance of the presented method. According to the numerical results, the method is convergent and energy stable, independent to the choice of time stepsize. Its MATLAB implementation is included in the appendix for the numerical evaluation of algorithm and reproduction of the presented results.

Keywords. Cahn-Hilliard system, MATLAB code, Multi Phase-field model, Schur complement, Space partitioning, Spinodal decomposition, Unconditionally energy stable.

Contents

1. Introduction

The Cahn-Hilliard energy functional has been introduced in [16] to approximate the total free energy of isolated inhomogeneous binary systems. Its conservative gradient flow, that is called the Cahn-Hilliard equation, has been derived in [14, 15] to study the spinodal decomposition in binary systems. In fact, the Cahn-Hilliard equation is the gradient flow of Cahn-Hilliard energy with respect to the H^{-1} inner product, c.f. [34]. The Cahn-Hilliard-like equations have been extensively employed in the literature to model second order phase transition phenomena, c.f. [54, 62]. The vector-valued Cahn-Hilliard equation, Cahn-Morral equation, has been introduced in [25, 26, 58] to model the spinodal decomposition in multi-component systems. The Cahn-Morral equation has been used in the literature to study the nucleation and growth, phase separation and coarsening in multi-component systems, for instance see: [8, 12, 18, 20, 28, 32, 43, 45, 46, 51, 53, 55, 59, 73].

Date: July 8, 2015.

Department of Materials Science and Engineering, Sharif University of Technology, Tehran, Iran, P.O. Box 11365-9466, tel: 982166165209, fax: 982166005717, email: rtavakoli@sharif.ir.

Due to the lack of analytical solution for the Cahn-Hilliard equation under general conditions, using numerical methods is very common to study the dynamics of Cahn-Hilliard equation. The euler explicit time integration approach [62] is the simplest method to solve this equation. Several computational methods have been invented in the literature to improve the accuracy, stability and/or efficiency of numerical solution of Cahn-Hilliard equation. For instance, exponential time differencing [22, 48], multigrid [49, 50, 80], adaptive time stepping [23, 36, 82, 84], isogeometric analysis [38, 57], C^1-continuity finite element [83], Semi-smooth Newton [11], Sobolev gradient [64–66, 72] approaches. See [77] as a recent survey on the numerical solution of Cahn-Hilliard equation.

Considering that the Cahn-Hilliard equation is a forth order parabolic PDE, the maximum allowable time stepsize during the numerical solution by conventional methods are severely restricted due to the stability of the numerical solution. To cope this problem, an unconditionally energy stable scheme has been introduced in [33] to solve the Cahn-Hilliard equation. In this method, the original energy functional was decomposed into a concave and a convex parts and their contribution in the Cahn-Hilliard equation was treated explicitly and implicitly respectively. According to [33], the resulting PDE is uniquely solvable and the energy functional reduces monotonically as time proceeds, independent to the size of time increments. Later, many works have been devoted for further analysis and extension of Eyre's approach to solve Cahn-Hilliard equation [17, 27, 42, 70, 71, 79, 84], Cahn-Hilliard equation with a fidelity term for image inpainting application [7, 68], nonlocal Cahn-Hilliard equation [40, 41], phase field crystal equation [19, 30, 37, 81] and equation corresponding to epitaxial growth simulation [63, 69]. The differences of these works stems in the difference between the spatial discretization approach, spatial and temporal accuracy and the way of concave-convex splitting of the corresponding energy functional. The later issue significantly changes the computational efficiency of the numerical algorithm. In the original treatment of Eyre [33], a nonlinear system of equations has to be solved every time step, which is computationally expensive. In [30, 68], the splitting approach was exploited such that a linear system of equation has to be solved per time step.

The existence of global solution for Cahn-Morral equation has been studied in [29]. There were several works on the numerical solution of Cahn-Morral equation, some instances are [3, 6, 8, 10, 12, 13, 20, 28, 39, 43, 44, 50, 52, 53, 55, 56, 59, 73]. However, there was few efforts on developing unconditionally gradient stable methods to solve Cahn-Morral equation. In [55] a practically unconditionally gradient stable scheme has been suggested to solve Cahn-Morral equation. The method was based on the discretization of the spatial domain by the finite difference method and temporal integration of resulted system of ordinary differential equations by a nonlinear splitting approach. It led to the solution of a nonlinear system of equations per time step that has been solved by a nonlinear multigrid solver.

In the present study, an unconditionally energy stable scheme is introduced to solve the Cahn-Morral equation. It requires the solution of a linear system of equations per time step. It is based on the combination of the Eyre's concave-convex splitting approach [31, 33] and the Schur complement method [67] to manage the pointwise incompressibility condition of phases. This method is used to model the spinodal decomposition in multicomponent systems with logarithmic homogeneous free energy density function. As it has been shown in [1], by the appropriate choice of nonlinear term in the energy functional, the sharp interface limit of Cahn-Morral energy converges to the total perimeter of a multiphase system under volume constraints. This idea has been used in [35, 61] to approximate the solution of the least perimeter periodic tessellation of space in two and three spatial dimensions. The method used in [35] was based on the solution of constrained Allen-Cahn equation. In [61], the projected nonlinear conjugate gradient method has been used directly to minimize the Cahn-Morral energy functional. The introduced method in the present study is adapted to approximately solve the least perimeter space tessellation problem too. Because a uniform concentration field is a local minimizer of the Cahn-Morral energy functional, a simple and effective penalization strategy is introduced in the this study to avoid the trivial solution. For this purpose, the Cahn-Morral energy functional is penalized by a term that approximates the standard deviation of the global minimizer of Cahn-Morral energy. The implementation of the

presented method is independent of the spatial discretization method. For the purpose of numerical experiment, the spatial discretization is performed based on the pseudo-spectral approach [78] in the present work. The success and performance of the introduced method is supported by extensive numerical experiments. According to our numerical results, the presented method is convergent and unconditionally energy stable without regard to the time step-size. Its MATLAB implementation is included within the appendix.

2. Cahn-Morral equation

The total free energy of an isolated inhomogeneous binary system can be approximated by the Cahn-Hilliard energy functional as follows [16]:

$$E(u) = \int_\Omega \left(\frac{\varepsilon}{2} \, |\nabla u|^2 + F(u) \right) d\mathbf{x} \tag{1}$$

where E denotes the total free energy, Ω denotes the spatial domain that is a bounded subset of $\mathbb{R}^d$ $(d = 2, 3)$ with sufficiently regular boundaries, u denotes the concentration field, ε is the gradient coefficient which is proportional to the interfacial energy and thickness of the (diffuse) interface between phases, and $F(u)$ denotes the free energy density of a homogeneous system with concentration $u(\mathbf{x})$. The gradient flow of (1) with respect to H^{-1} inner product leads to the Cahn-Hilliard equation:

$$\frac{\partial u}{\partial t} = -\Delta\big(\varepsilon\Delta u - f(u)\big), \quad (\mathbf{x}, t) \in \Omega \times \mathcal{T}, \quad u(\mathbf{x}, 0) = u_0, \quad \partial_n u|_{\partial\Omega} = \partial_n\big(\varepsilon\Delta u - f(u)\big)|_{\partial\Omega} = 0 \tag{2}$$

where Δ denotes the laplacian operator, $f(u) = F'(u)$, $\mathcal{T} = [0, T]$ denotes the temporal domain, $\partial\Omega$ denotes the boundaries of Ω, $\partial_n u := \nabla u \cdot \mathbf{n}$ and $\mathbf{n}$ denotes the outward unit normal on $\partial\Omega$.

The multicomponent version of Cahn-Hilliard energy functional, that is called the Cahn-Morral energy functional here, can be expressed as follows [10, 28, 29, 55, 61, 75]:

$$\mathbf{E}(\mathbf{u}) := \sum_{i=1}^{p} \int_\Omega \frac{\varepsilon}{2} \, |\nabla u_i|^2 \, d\mathbf{x} + \int_\Omega \mathbf{F}(\mathbf{u}) \, d\mathbf{x} \tag{3}$$

where $p \geqslant 2$ denotes the number of phases, u_i denotes the concentration field corresponding to i-th phase, $\mathbf{u} := (u_1, \ldots, u_p)^T$ denotes the vector valued concentration field and $\mathbf{F}(\mathbf{u}(\mathbf{x}))$ denotes the free energy density of a homogeneous system with concentration $\mathbf{u} = \mathbf{u}(\mathbf{x})$. There are many possible choices for the function $\mathbf{F}$. However, the logarithmic free energy [2–6, 10, 20, 24, 29] and symmetric p-well function [55, 61, 74, 75] are two common choices which are extensively used in the literature. They are respectively expressed as follows:

$$\mathbf{F}_L(\mathbf{u}) = \frac{-1}{2} \, \mathbf{u}^T \mathbf{A} \mathbf{u} + \theta \sum_{i=1}^{p} u_i \ln u_i \tag{4}$$

$$\mathbf{F}_W(\mathbf{u}) = \frac{1}{4} \, \sum_{i=1}^{p} u_i^2 (u_i - 1)^2 \tag{5}$$

where $\theta \in \mathbb{R}^+$ is a constant and $\mathbf{A} \in \mathbb{R}^{p \times p}$ is a symmetric non-negative definite matrix, i.e., it has at least one positive eigenvalue. Although our algorithm can be equivalently applied for an arbitrary choice of function $\mathbf{F}$, we will use $\mathbf{F}_L$ and $\mathbf{F}_W$ in this study to demonstrate the utility of the presented algorithm. Following [2–6, 10, 20], we use

$$\mathbf{A} = -\theta_c \, (\mathbf{1}\mathbf{1}^T - \mathbf{I}) \tag{6}$$

in the present study, where $\theta_c \in \mathbb{R}^+$, $\mathbf{1} \in \mathbb{R}^p$ denotes a vector with all entries equal to unity and $\mathbf{I} \in \mathbb{R}^{p \times p}$ denotes the identity matrix. For instance when $p = 3$, matrix $\mathbf{A}$ can be expressed as follows:

$$\mathbf{A} = -\theta_c \begin{pmatrix} 0 & 1 & 1 \\ 1 & 0 & 1 \\ 1 & 1 & 0 \end{pmatrix}$$

Substituting (6) into (4) results in:

$$\mathbf{F}_L(\mathbf{u}) = \theta \sum_{i=1}^{p} u_i \ln u_i + \theta_c \sum_{i=1}^{p} \sum_{j=i+1}^{p} u_i u_j \tag{7}$$

Because, u_i denotes the concentration of the i-th phase, it should satisfies the following pointwise consttaint:

$$0 \leqslant u_i \leqslant 1, \quad i = 1, \ldots, p \tag{8}$$

Although there are a few works in which the above set of constraints are directly taken into account during the minimization of (3) (cf. [9, 35, 60, 74, 75]), they are commonly managed indirectly during the numerical solution. For instace, $\mathbf{u}$ is projected onto (8) after every time step. Unlike the two-phase case, there are additional pointwise constraints due to the incompressibility of phases, i.e. the sum of concentration fields at every point $\mathbf{x} \in \Omega$ should be equal to unity:

$$\sum_{i=1}^{p} u_i = 1 \tag{9}$$

Assuming there is no reaction in the system, there are p volume constraints on the total measure of each phase inside Ω:

$$\int_{\Omega} u_i \; d\mathbf{x} = \Lambda_i |\Omega|, \quad i = 1, \ldots, p \tag{10}$$

where Λ_i $(i = 1, \ldots, p)$ is equal to the total volume fraction of i-th phase in Ω. Obviously $0 \leqslant \Lambda_i \leqslant 1$ and $\sum_{i=1}^{p} \Lambda_i = 1$. Assuming the initial concentration field, denoted by $\mathbf{u_0} = \{u_{1,0}, \ldots, u_{p,0}\}$ satisfies (10), then we have: $\Lambda_i = \big(\int_{\Omega} u_{i,0}(\mathbf{x}) \; d\mathbf{x}\big)/|\Omega|$ for $i = 1, \ldots, p$.

Considering pointwise constraints (9), the H^{-1} gradient flow of (3) results in the following system of equations, denoted by Cahn-Morral equation henceforth:

$$\frac{\partial u_i}{\partial t} = -\Delta\big(\varepsilon \Delta u_i - f_i(\mathbf{u})\big) + \Delta\big(\varepsilon \Delta u_p - f_p(\mathbf{u})\big), \quad \texttt{in} \quad \Omega, \quad \texttt{for i} = 1, \ldots, \texttt{p} - 1 \tag{11}$$

with boundary conditions

$$\partial_n u_i = \partial_n\big(\varepsilon \Delta u_i - f_i(\mathbf{u})\big) = 0 \quad \texttt{on} \quad \partial\Omega \tag{12}$$

and initial conditions $\mathbf{u}(\mathbf{x}, t = 0) = \mathbf{u_0}$, where $f_i(\mathbf{u}) = \partial \mathbf{F}(\mathbf{u})/\partial u_i$ for $\texttt{i} = 1, \ldots, \texttt{p} - 1$, $\mathbf{F}$ is equal to either of $\mathbf{F}_L$ or $\mathbf{F}_W$, and,

$$u_p = 1 - \sum_{i=1}^{p-1} u_i \tag{13}$$

It is well known that if $\mathbf{u_0}$ satisfies constraints (10) then solution of (11) satisfies (10) as well. In fact (11) does the minimization on the null space of constraints (10), cf. section 2 of [34]. Furthermore, by (13) pointwise constraints (9) will be satisfied naturally. It is obvious that when constraints (10) holds the nonnegativity of u_i is sufficient to ensure the feasibility of solutions with respect to constraints (8). According to our numerical experience, when the numerical scheme is energy stable, the nonnegativity constraints naturally holds. Therefore, we do not attend to ensure the feasibility of solutions with respect to left hand side inequalities in (8).

3. Unconditionally energy stable time stepping scheme for Cahn-Morral equation

Considering the energy functional (3), the first term is convex, however, the second term is not convex under general conditions, for instance with the choice of either of (5) and (7). Therefore, it not only admits possibly multiple minimizers but also the stability of its time discretized gradient flow depends on the size of time increment. The later issue commonly leads to a severe restriction on the maximum allowable time stepsize of the numerical solution. To avoid this problem, the Eyre's unconditionally gradient stable approach [31, 33] will be combined with the Schur complement method (c.f. section 14.2 of [67]) in this section to solve the Cahn-Morral equation.

According to [31, 33], if the energy functional is decomposed into a convex and concave parts and the gradient flow of convex and concave parts are respectively treated implicitly and explicitly

during the numerical time integration, then the gradient flow will be unconditionally energy stable under some mild conditions. There are many possible choices for the mentioned decomposition. However, because the gradient flow of convex part should be treated implicitly, it is desirable to do the decomposition such that it leads to the solution of a linear system of equations per time step. Inspiring from [30], the following convex-concave decomposition is used in the present study:

$$\mathbf{E}(\mathbf{u}) = \mathbf{E}_c(\mathbf{u}) - \mathbf{E}_e(\mathbf{u}) \tag{14}$$

$$\mathbf{E}_c(\mathbf{u}) := \sum_{i=1}^{p} \int_\Omega \frac{\varepsilon}{2} \, |\nabla u_i|^2 \, d\mathbf{x} + \frac{c}{2} \, \|\mathbf{u}\|_H^2 \tag{15}$$

$$\mathbf{E}_e(\mathbf{u}) := \frac{c}{2} \, \|\mathbf{u}\|_H^2 - \int_\Omega \mathbf{F}(\mathbf{u}) \, d\mathbf{x} \tag{16}$$

where parameter $c \in \mathbb{R}^+$ controls the quality of the decomposition and H denotes the function space that is occupied with measurable functions with respect to the following norm:

$$\|\mathbf{u}\|_H^2 := \alpha \, \sum_{i=1}^{p} \int_\Omega u_i^2 \, d\mathbf{x} + \beta \, \sum_{i=1}^{p} \int_\Omega |\nabla u_i|^2 \, d\mathbf{x} \tag{17}$$

where $\alpha, \beta \in \mathbb{R}$, $\alpha, \beta \geqslant 0$ and $\alpha + \beta > 0$. In fact, when $(\alpha, \beta) = (1, 0)$, $H = \big(L^2(\Omega)\big)^p$. On the other hand, when $(\alpha, \beta) = (0, 1)$, $\| \cdot \|_H$ is the semi-norm of $\big(H^1(\Omega)\big)^p$. Finally, when $\alpha = \beta = 1$ or more generally when $\alpha, \beta > 0$, $\| \cdot \|_H$ defines a norm on $\big(H^1(\Omega)\big)^p$. When c is sufficiently large, energy functionals $\mathbf{E}_c$ and $\mathbf{E}_e$ are convex. Therefore, the Eyre's approach can be applied to the splitting (14) when c is sufficiently large.

Assume the temporal domain is discretized into a uniform grid with time stepsize τ. Furthermore, assume that the superscript n denotes the time level, i.e. X^n denotes the field variable X at $t = n\tau$. Applying the Eyre's scheme to (14) results in (c.f. [31]):

$$\frac{u_i^{n+1} - u_i^n}{\tau} = -\nabla_i \, \mathbf{E}_c(\mathbf{u}^{n+1}) + \nabla_i \, \mathbf{E}_e(\mathbf{u}^n), \qquad \texttt{for} \quad i = 1, \ldots, p-1 \tag{18}$$

where operator $\nabla_i(\cdot)$ denotes the H^{-1} variational derivative operator with respect to u_i (c.f. [34]):

$$\nabla_i \, \mathbf{E}_c(\mathbf{u}^{n+1}) = \Delta\big((\varepsilon + c\beta) \, \Delta u_i^{n+1} - c\alpha \, u_i^{n+1}\big) - \Delta\big((\varepsilon + c\beta) \, \Delta u_p^{n+1} - c\alpha \, u_p^{n+1}\big) \tag{19}$$

$$\nabla_i \, \mathbf{E}_e(\mathbf{u}^n) = \Delta\big(c\beta \, \Delta u_i^n - c\alpha \, u_i^n\big) - \Delta\big(c\beta \, \Delta u_p^n - c\alpha \, u_p^n\big) + \Delta\big(f_i(\mathbf{u}^n) - f_p(\mathbf{u}^n)\big) \tag{20}$$

and u_p^{n+1} is computed by the following equation:

$$u_p^{n+1} = 1 - \sum_{i=1}^{p-1} u_i^{n+1} \tag{21}$$

Considering $\mathbf{F} = \mathbf{F}_L, \ \mathbf{F}_W$ according to (7) and (5), we have:

$$f_i(\mathbf{u}^n) = \theta \, (1 + \ln u_i^n) + \theta_c \sum_{j=1, \ j \neq i}^{p} u_j^n, \quad \texttt{for} \quad \mathbf{F} = \mathbf{F}_L \tag{22}$$

$$f_i(\mathbf{u}^n) = (u_i^n)^3 - \frac{3}{2} \, (u_i^n)^2 + \frac{1}{2} \, u_i^n, \quad \texttt{for} \quad \mathbf{F} = \mathbf{F}_W \tag{23}$$

Using simple algebra results in:

$$f_i(\mathbf{u}^n) - f_p(\mathbf{u}^n) = \theta \, (\ln u_i^n - \ln u_p^n) - \theta_c \, (u_i^n - u_p^n) =: f_{L,i}(u_i^n, u_p^n), \quad \texttt{for} \quad \mathbf{F} = \mathbf{F}_L \tag{24}$$

$$f_i(\mathbf{u}^n) - f_p(\mathbf{u}^n) = (u_i^n)^3 - (u_p^n)^3 - \frac{3(u_i^n)^2}{2} + \frac{3(u_p^n)^2}{2} + \frac{u_i^n}{2} - \frac{u_p^n}{2} =: f_{W,i}(u_i^n, u_p^n), \ \ \texttt{for} \ \ \mathbf{F} = \mathbf{F}_W \tag{25}$$

Therefore, $f_i(\mathbf{u}^n) - f_p(\mathbf{u}^n)$ is a function of u_i^n and u_p^n for both forms of $\mathbf{F}(\mathbf{u})$ considered in the present study. By substituting (19)-(20) and (22)-(24) into (18) and simple algebra, (18) can be written in the following abstract form:

$$\big(\mathcal{I} + \tau\mathcal{L}_c\big)\ u_i^{n+1} - \tau\mathcal{L}_c u_p^{n+1} = u_i^n + \tau\mathcal{N}(u_i^n, u_p^n), \qquad i = 1, \ldots, p-1 \tag{26}$$

where $\mathcal{I}$ denotes the identity operator, $\mathcal{L}_c := \big((\varepsilon + c\beta)\ \Delta^2 - c\alpha\ \Delta\big)$ and

$$\mathcal{N}(u_i^n, u_p^n) := \mathcal{L}_e\big(u_i^n - u_p^n\big) + \Delta\big(f_{X,i}(u_i^n, u_p^n)\big) \tag{27}$$

where $\mathcal{L}_e := \big(c\beta\ \Delta^2 - c\alpha\ \Delta\big)$ and $X = L,\ W$ for $F = F_L,\ F_W$ respectively. Equations (21) and (26) can be expressed in the following matrix form:

$$\begin{pmatrix} \mathcal{A} & 0 & \cdots & \cdots & \mathcal{B} \\ 0 & \mathcal{A} & 0 & \cdots & \mathcal{B} \\ \vdots & 0 & \ddots & \ddots & \vdots \\ \vdots & \vdots & \ddots & \mathcal{A} & \mathcal{B} \\ \mathcal{I} & \mathcal{I} & \cdots & \mathcal{I} & \mathcal{I} \end{pmatrix} \begin{pmatrix} u_1^{n+1} \\ u_2^{n+1} \\ \vdots \\ u_{p-1}^{n+1} \\ u_p^{n+1} \end{pmatrix} = \begin{pmatrix} r_1^n \\ r_2^n \\ \vdots \\ r_{p-1}^n \\ 1 \end{pmatrix} \tag{28}$$

where $\mathcal{A} := \mathcal{I} + \tau\mathcal{L}_c$, $\mathcal{B} := -\tau\mathcal{L}_c$ and $r_i^n := u_i^n + \tau\mathcal{N}(u_i^n, u_p^n)$ for $i = 1, \ldots, p-1$. Exploiting the sparse structure of above linear system of PDEs, it is easy to solve it efficiently by means of Schur complement approach (c.f. section 14.2 of [67]). Applying the Schur complement method to system (28), the Schur complement operator, $\mathcal{S}$ is defined as follows:

$$\mathcal{S} = \mathcal{I} - (p-1)\ \mathcal{A}^{-1}\mathcal{B} \tag{29}$$

Then, u_p^{n+1} and vector $(u_1^{n+1}, \ldots, u_{p-1}^{n+1})^T$ are computed sequentially by the following equations:

$$u_p^{n+1} = \mathcal{S}^{-1}\bigg(1 - \sum_{i=1}^{p-1}\big(\mathcal{A}^{-1}\ r_i^n\big)\bigg) \tag{30}$$

$$u_i^{n+1} = \mathcal{A}^{-1}\Big(r_i^n - \mathcal{B}\ u_p^{n+1}\Big), \quad \texttt{for}\ \ i = 1, \ldots, p-1 \tag{31}$$

Assuming, time stepsize is fixed during the numerical solution, then, the linear differential operators $\mathcal{A}$, $\mathcal{B}$ and $\mathcal{S}$ are fixed in the course of simulation. Therefore, it is sufficient to compute these operators once prior to the time stepping procedure and reuse them during time increments. Considering (30) and (31), $2p-1$ number of linear system of equations should be solved to compute $\mathbf{u}$. To reduce the computational cost of these steps, it is reasonable to compute the LU factorization of matrices corresponding to the spatial discretization of operators $\mathcal{A}$ and $\mathcal{S}$ before the time stepping, and then use these factors during subsequent numerical procedure.

Although the presented algorithm is independent to the choice of spatial discretization scheme that applied to the differential operators, under the assumption of periodic boundary conditions, the pseudo-spectral approach [78] based on the fast fourier transform (FFT) is used in this work to study the behavior of algorithm in practice. Because the discretized form of laplacian operator will be a diagonal matrix in the Fourier space, the solutions of mentioned system of equations reduce to a simple inner product in the Fourier space. Therefore, the computational complexity of the presented algorithm per time step will of order $\mathtt{M}\log\mathtt{M}$, where $\mathtt{M}$ denotes the total number of degrees of freedom after the spatial discretization. Note that we do not theoretically prove the unconditional gradient stability of above algorithm in this paper, but we will demonstrate it practically by means of numerical experiments. However, we believe that it should not be difficult to prove its stability under mild conditions using methods similar to that of [30, 31, 68, 81].

Because the derivation of algebraic system of equations after the spatial discretization is trivial (c.f. [78]), we do not present it here for the purpose of brevity. Interested readers are referred to the appendix of this paper in which the MATLAB implementation of our algorithm is included.

4. Penalization of energy functional by the standard deviation

Assume that $\mathbf{F} = \mathbf{F}_W$ in this section. According to [1, 61], when $\varepsilon \to 0$, (3) Γ-converges to the total perimeter between phases in Ω. In fact, the sharp interface limit of (3) is equal to the total perimeter of phases. Therefore, minimization of (3) can be used to solve the least perimeter space partitioning problem.This problem has been extensively study in the literature. For instance, it is studied numerically in two spatial dimensions by a discrete graph-based approach in [21]. In [61], this problem is solved in two and three spatial dimensions using a continuum approximation based on the constrained minimization of (3). Following [61], in the present study, we use the constrained minimization of (3) to approximately solve the least perimeter space tilling problem. However, because (3) is non-convex, it is very likable that the minimization path of (3) converges to the uniform concentration field, more precisely uniform mixing of phases in the spatial domain. Note that when the uniform concentration field is a trivial constrained stationary point of (3). According to our numerical experiments, this problem commonly happens for $p \geqslant 5$, in particular if $\mathbf{u_0}$ is considered as the small amplitude random perturbation from the uniform concentration field.

To avoid this problem, we use the penalization of (3) by the mismatch between the standard deviation of the numerical solution and its sharp interface limit (expected solution). For a discrete set $y = \{y_1, y_2, \dots, y_N\}$, the standard deviation, σ, is defined as follows:

$$\sigma = \sqrt{\frac{1}{N}\sum_{i=1}^{N}(y_i - \bar{y})^2}, \qquad \bar{y} = \frac{1}{N}\sum_{i=1}^{N} y_i$$

Similarly, if y is a continuous set (field) defined on the spatial domain Ω, i.e. $y = y(\mathbf{x})$, the standard deviation can be computed as follows:

$$\sigma = \sqrt{\frac{1}{|\Omega|}\int_{\Omega}(y - \bar{y})^2 \, dx}, \qquad \bar{y} = \frac{1}{|\Omega|}\int_{\Omega} y \, dx$$

Consider, the optimal space partitioning problem in which the goal is to decompose Ω into p number of non-overlapping sub-domains Ω_i with a-priori known measure $|\Omega_i|$ (for $i = 1, \dots, p$) such that the total boundaries between sub-domains is minimized. Furthermore, consider the vector field $\mathbf{v} = (v_1, \dots, v_p)^T$ includes the characteristic functions of Ω_i (for $i = 1, \dots, p$), i.e. $v_i(x) = 1$ if $x \in \Omega_i$ and $v_i(x) = 0$ if $x \in \Omega \setminus \Omega_i$. Assume $\mathbf{v}^* = (v_1^*, \dots, v_p^*)^T$ denotes the optimal solution of this space partitioning problem. Then, as it is shown below, the standard deviation of v_i^* (for $i = 1, \dots, p$), denoted by σ_i^* here, can be computed without any knowledge about the optimal solution. It is easy to show that the mean value of v_i^* is equal to $|\Omega_i|/|\Omega|$, that is denoted by Λ_i in the present study. For σ_i^* we have:

$$\begin{aligned}
\sigma_i^* &= \sqrt{\frac{1}{|\Omega|}\int_{\Omega}(v_i^* - \Lambda_i)^2 \, dx} = \sqrt{\frac{1}{|\Omega|}\int_{\Omega_i}(v_i^* - \Lambda_i)^2 \, dx + \int_{\Omega\setminus\Omega_i}(v_i^* - \Lambda_i)^2 \, dx} \\
&= \sqrt{\frac{1}{|\Omega|}\left[\int_{\Omega_i}(1 - \Lambda_i)^2 \, dx + \int_{\Omega\setminus\Omega_i}\Lambda_i^2 \, dx\right]} = \sqrt{\frac{|\Omega_i|}{|\Omega|}(1 - \Lambda_i)^2 + \frac{|\Omega| - |\Omega_i|}{|\Omega|}\Lambda_i^2} \\
&= \sqrt{\Lambda_i(1 - \Lambda_i)}
\end{aligned} \tag{32}$$

Considering the fact that v_i^* is the sharp interface limit of constrained minimizers of (3), we use the standard deviation of v_i^* as an approximation for the standard deviation of minimizers of (3). Therefore, we penalize the energy functional $\mathbf{E}(\mathbf{u})$ with the mismatch function between the standard deviation of $\mathbf{u}$ and that of $\mathbf{v}^*$. Then, we do the constrained minimization of penalized functional $\mathbf{E}_\zeta$ instead of (3):

$$\mathbf{E}_\zeta(\mathbf{u}) := \mathbf{E}(\mathbf{u}) + \zeta P(\mathbf{u}) \tag{33}$$

where $\zeta \geqslant 0$ is the penalization parameter and,

$$P(\mathbf{u}) := \frac{1}{2}\sum_{i=1}^{p}\left(\sigma_i - \sigma_i^*\right)^2 \tag{34}$$

where σ_i^* is computed according to (32) and,

$$\sigma_i = \sqrt{\frac{1}{|\Omega|}\int_\Omega (u_i - \Lambda_i)^2 \, dx} \tag{35}$$

Considering pointwise constraints (9), the H^{-1} gradient flow of (33) leads to the Cahn-Morral equation similar to (11), except $f_i(\mathbf{u})$ (for $i = 1, \ldots, p$) is replaced by $f_{\zeta,i}(\mathbf{u})$, where $f_{\zeta,i}(\mathbf{u}) = \partial \mathbf{F}_\zeta(\mathbf{u})/\partial u_i$ (for $\mathtt{i} = \mathtt{1}, \ldots, \mathtt{p-1}$), and,

$$\mathbf{F}_\zeta(\mathbf{u}) := \mathbf{F}(\mathbf{u}) + \zeta P(\mathbf{u}) \tag{36}$$

By straightforward derivation we have:

$$f_{\zeta,i}(\mathbf{u}) = f_i(\mathbf{u}) + \frac{\zeta}{|\Omega|}\,\frac{(\sigma_i - \sigma_i^*)}{\sigma_i}\,(u_i - \Lambda_i) \tag{37}$$

Therefore, the unconditionally gradient stable algorithm developed in section 3 for the constrained minimization of $\mathbf{E}(\mathbf{u})$ can be equivalently applied to the minimization of $\mathbf{E}_\zeta(\mathbf{u})$ under the corresponding constraints. In fact, it is sufficient to replace r_i^n (for $i = 1, \ldots, p-1$) in (30) and (31) with $r_{\zeta,i}^n$ (for $i = 1, \ldots, p-1$) and use the same solution algorithm as discussed in section 3, where,

$$r_{\zeta,i}^n := r_i^n + \frac{\tau\zeta}{|\Omega|}\,\Delta\left(\frac{(\sigma_i - \sigma_i^*)}{\sigma_i}\,(u_i - \Lambda_i) - \frac{(\sigma_p - \sigma_p^*)}{\sigma_p}\,(u_p - \Lambda_p)\right) \tag{38}$$

As it is shown in our numerical experiments, the penalization strategy introduced in this section effectively bypasses the trapping of minimization path into the trivial constrained stationary point of $\mathbf{E}(\mathbf{u})$ when the penalization parameter ζ is chosen appropriately.

5. Results and discussion

In this section we will study the success and performance of the presented algorithm by means of numerical experiments. A personal computer with an Intel Core i5-4690 3.5 GHz processor and 4.0 GB RAM is used as the computational resource in this section. For the evaluation of the presented algorithm, 164 two dimensional test cases are considered in this section. Among them the first 114 cases are related to the choice of logarithmic homogeneous free energy density and the remainders are corresponding to the polynomial multi-well function. In all cases Ω is assumed to be a square domain with edge length equal to $\mathtt{nx}$, i.e. $\Omega = [0, \mathtt{nx}]^2$ and the periodic boundary condition is applied on its borders. The spatial domain is discretized into $\mathtt{nx} \times \mathtt{nx}$ uniform grid and the FFT algorithm is used for the approximation of differential operators. In all cases the simulation is terminated whenever the number of iterations reaches to the maximum bound $\mathtt{iterm}$. The temporal domain varies case by case based on the choice of tim stepsize (τ) and $\mathtt{iterm}$. A uniform concentration field with a small amplitude random perturbation is considered as the initial condition in every test case, i.e. $\mathbf{u_0}(\mathbf{x}) = (\Lambda_1, \ldots, \Lambda_p)^T + \varsigma\rho$, where ς is a small positive constant and ρ denotes a random number generated uniformly in interval $[-1, 1]$. Because our minimization problem is non-convex, its optimal solution is a function of the initial condition. Due to this fact, in cases #115-#162 where the global minimizer of the functional is desired, each case is run five times and within them, the solution with the least value of the energy functional is reported here. In all cases ε is taken equal to the grid size, i.e. $\varepsilon = 1$. Other simulation parameters corresponding to test cases #1-#164 are mentioned later in this section. To plot the distribution of phases, RGB coloring MATLAB function developed in [76] is used here. For this purpose we assign colors red, blue, green and yellow to phases 1, 2, 3 and 4 respectively.

Following [10], in test cases #1-#60, $\mathbf{F} = \mathbf{F_L}$ with $\theta = 0.3$, $\theta_c = 1$. Moreover, $p = 3$, $(\alpha, \beta) = (1, 0)$, $\varsigma = 0.05$, $(\Lambda_1, \Lambda_2, \Lambda_3) = (0.15, 0.2, 0.65)$, $\zeta = 0$, $\mathtt{nx} = 512$, $\mathtt{iterm} = 2000$. The time stepsize and c respectively vary from 1 to 10^5 and 1 to 10 in cases #1-#60 as listed in table 1. In fact,

this example models the liquid state spinodal decomposition in a ternary system. According to linear stability analysis has been done in [10], the assumed initial value is unstable and the initial concentration field should be decomposed into three separate phases as time proceeds (this problem also solved in section 5.2 of [6]). The values of energy functional at the end of simulation (iteration 2000) are shown in table 2. The `NaN` symbol in this table denotes the divergence of numerical solution. According to the table the algorithm was convergent except for a few cases in which c is not sufficiently large. Therefore, the method behaves as it is expected from the theory. Considering table 2, the best computational performance is attained for test case #23. Moreover, the efficiency of the presented algorithm firstly increases by increasing c and τ, however, it starts to decay when they reach to sufficiently large values. These observations imply that using a large time stepsize does not always leads to the best computational efficiency, but there is an optimal choice for binary (c, τ). In fact, as it is discussed in [19, 47], there is an effective time stepsize for the numerical algorithm for every choice of c. To study the convergence of algorithm, figure 1 shows the variation of energy functional with iteration for test cases #19-#24 ($c = 4$ and different values of τ). Similarly figure 2 shows the variation of energy functional with iteration for test cases #8, #20, #32, #44 and #56 ($\tau = 10$ and different values of c). According to the plots, the energy is decreased monotonically in all cases. It numerically confirms the convergence and energy stability of the presented algorithm. Figure 3 shows the distribution of phases, $\mathbf{u}(\cdot, t)$, at different iterations (times) for test cases #19-#23. According to the figure the phases are separated and start to coarsening, in agreement to the linear stability analysis theory (c.f. section 4 of [10]).

case	c	τ	case	c	τ	case	c	τ	case	c	τ	case	c	τ
#1	1	10^0	#13	3	10^0	#25	5	10^0	#37	7	10^0	#49	9	10^0
#2	1	10^1	#14	3	10^1	#26	5	10^1	#38	7	10^1	#50	9	10^1
#3	1	10^2	#15	3	10^2	#27	5	10^2	#39	7	10^2	#51	9	10^2
#4	1	10^3	#16	3	10^3	#28	5	10^3	#40	7	10^3	#52	9	10^3
#5	1	10^4	#17	3	10^4	#29	5	10^4	#41	7	10^4	#53	9	10^4
#6	1	10^5	#18	3	10^5	#30	5	10^5	#42	7	10^5	#54	9	10^5
#7	2	10^0	#19	4	10^0	#31	6	10^0	#43	8	10^0	#55	10	10^0
#8	2	10^1	#20	4	10^1	#32	6	10^1	#44	8	10^1	#56	10	10^1
#9	2	10^2	#21	4	10^2	#33	6	10^2	#45	8	10^2	#57	10	10^2
#10	2	10^3	#22	4	10^3	#34	6	10^3	#46	8	10^3	#58	10	10^3
#11	2	10^4	#23	4	10^4	#35	6	10^4	#47	8	10^4	#59	10	10^4
#12	2	10^5	#24	4	10^5	#36	6	10^5	#48	8	10^5	#60	10	10^5

TABLE 1. The values of τ and c in test cases #1-#60.

case	**E**	case	**E**	case	**E**	case	**E**	case	**E**
#1	NaN	#13	−3279	#25	−3235	#37	−3278	#49	−3250
#2	NaN	#14	−4681	#26	−4520	#38	−4452	#50	−4401
#3	NaN	#15	−5401	#27	−5219	#39	−5137	#51	−5114
#4	NaN	#16	−5774	#28	−5465	#40	−5409	#52	−5389
#5	NaN	#17	−5789	#29	−5717	#41	−5672	#53	−5408
#6	NaN	#18	−5874	#30	−5747	#42	−5594	#54	−5515
#7	−3292	#19	−3264	#31	−3251	#43	−3277	#55	−3272
#8	−4666	#20	−4494	#32	−4471	#44	−4452	#56	−4359
#9	NaN	#21	−5375	#33	−5227	#45	−5130	#57	−5079
#10	NaN	#22	−5579	#34	−5529	#46	−5353	#58	−5255
#11	NaN	#23	−5796	#35	−5713	#47	−5443	#59	−5386
#12	NaN	#24	−5785	#36	−5582	#48	−5454	#60	−5414

TABLE 2. The energy functional values at iteration 2000 for test cases #1-#60.

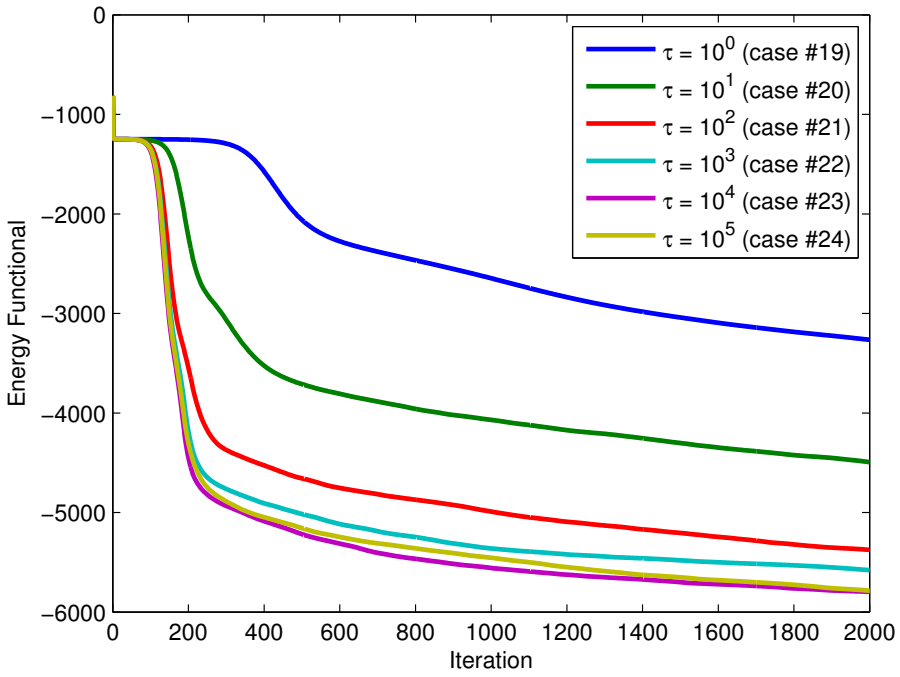

FIGURE 1. The variation of energy function with iteration for test cases #19-#24 (c is equal to 4 and τ varies from 1 to 10^5).

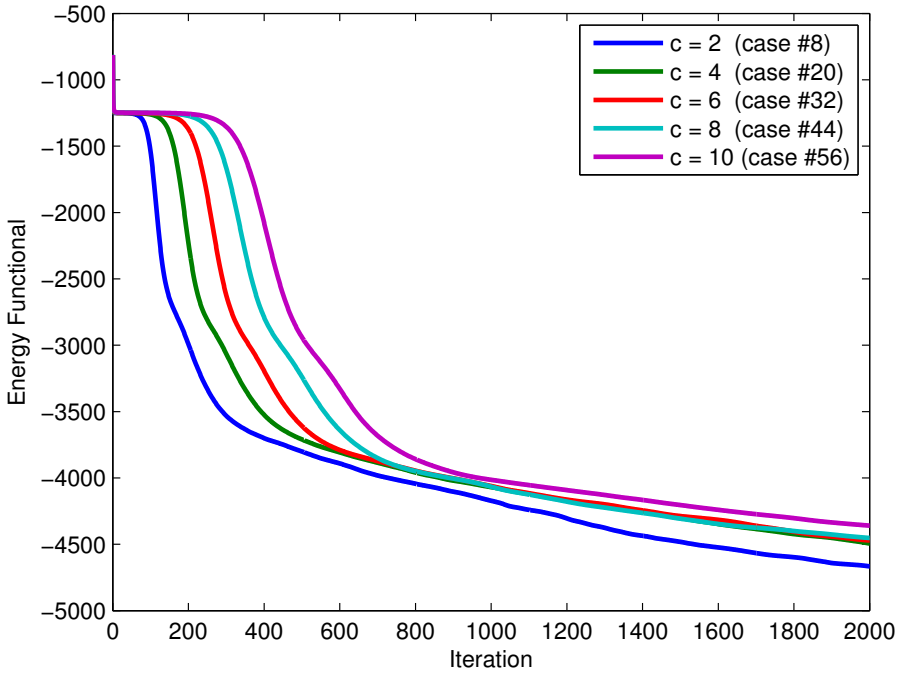

FIGURE 2. The variation of energy function with iteration for test cases #8, #20, #32, #44 and #56 (τ is equal to 10 and c varies from 2 to 10).

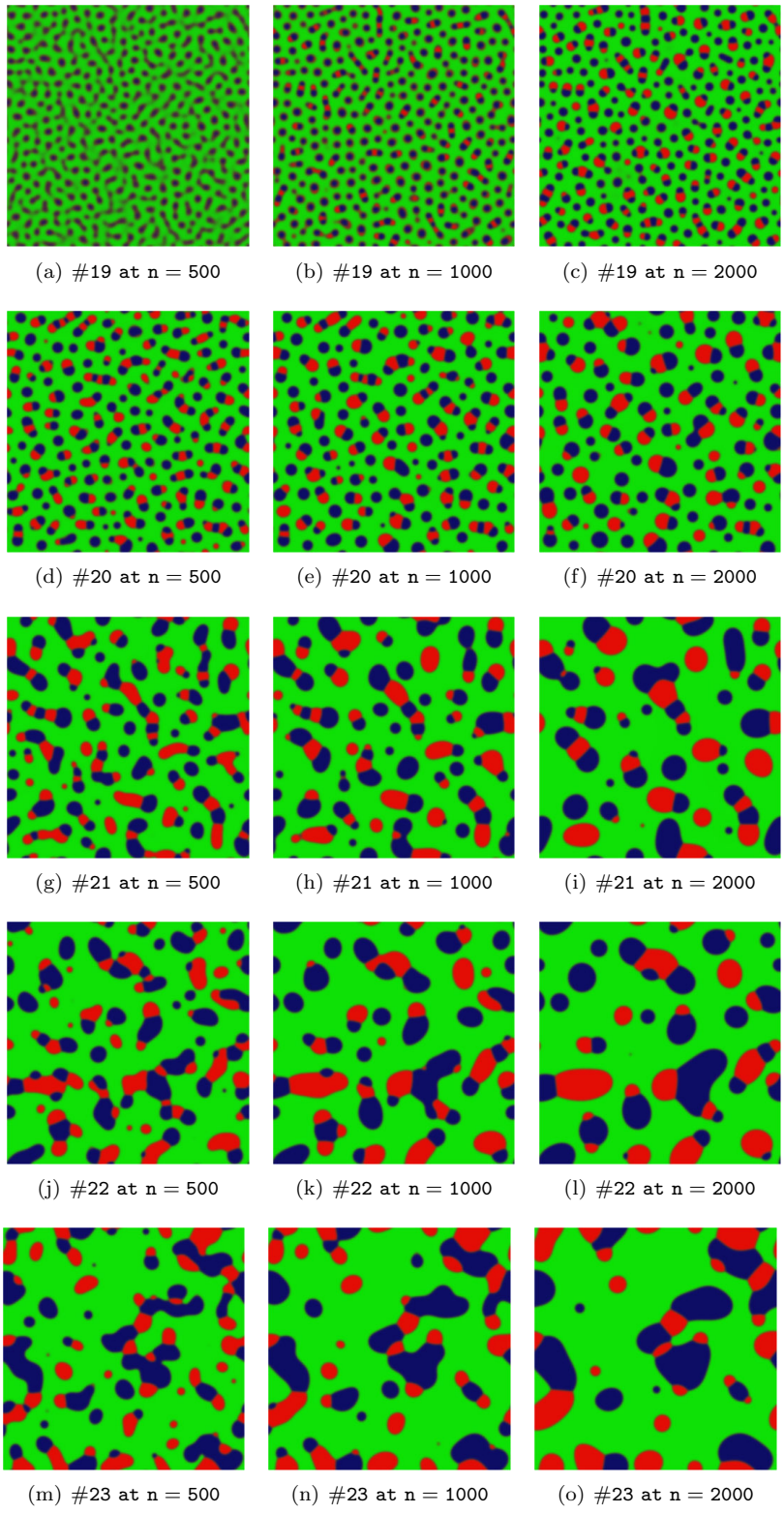

(a) #19 at n = 500 (b) #19 at n = 1000 (c) #19 at n = 2000

(d) #20 at n = 500 (e) #20 at n = 1000 (f) #20 at n = 2000

(g) #21 at n = 500 (h) #21 at n = 1000 (i) #21 at n = 2000

(j) #22 at n = 500 (k) #22 at n = 1000 (l) #22 at n = 2000

(m) #23 at n = 500 (n) #23 at n = 1000 (o) #23 at n = 2000

FIGURE 3. **u** at iterations 500, 1000 and 2000 for test cases #19-#23.

In test cases #61-#84 all simulation parameters are similar to test cases #1-#60, except $(\alpha, \beta) = (0, 1)$. Furthermore, the time stepsize and c respectively vary from 1 to 10^3 and 1 to 100 in these test cases, as listed in table 3. The values of energy functional at the end of simulation (iteration 2000) are presented in table 4. Figure 4 shows the variation of energy functional with iteration for test cases #70, #74, #78 and #82 ($\tau = 10$ and different values of c). According to these results for $(\alpha, \beta) = (0, 1)$ the value of c should be more than an order of magnitude larger than case $(\alpha, \beta) = (1, 0)$. Furthermore, the method is convergent and energy stable when c is sufficiently large. Figure 5 shows the distribution of phases at different iterations for test cases #70, #74, #78 and #82.

case	c	τ	case	c	τ	case	c	τ	case	c	τ	case	c	τ	case	c	τ
#61	1	10^0	#65	10	10^0	#69	20	10^0	#73	40	10^0	#77	80	10^0	#81	100	10^0
#62	1	10^1	#66	10	10^1	#70	20	10^1	#74	40	10^1	#78	80	10^1	#82	100	10^1
#63	1	10^2	#67	10	10^2	#71	20	10^2	#75	40	10^2	#79	80	10^2	#83	100	10^2
#64	1	10^3	#68	10	10^3	#72	20	10^3	#76	40	10^3	#80	80	10^3	#84	100	10^3

TABLE 3. The values of τ and c in test cases #61-#84.

case	**E**	case	**E**	case	**E**	case	**E**	case	**E**	case	**E**
#61	NaN	#65	−3292	#69	−3310	#73	−3309	#77	−3397	#81	−3434
#62	NaN	#66	NaN	#70	−4535	#74	−4466	#78	−4495	#82	−4468
#63	NaN	#67	NaN	#71	NaN	#75	NaN	#79	NaN	#83	NaN
#64	NaN	#68	NaN	#72	NaN	#76	NaN	#80	NaN	#84	NaN

TABLE 4. The energy functional values at iteration 2000 for test cases #61-#84.

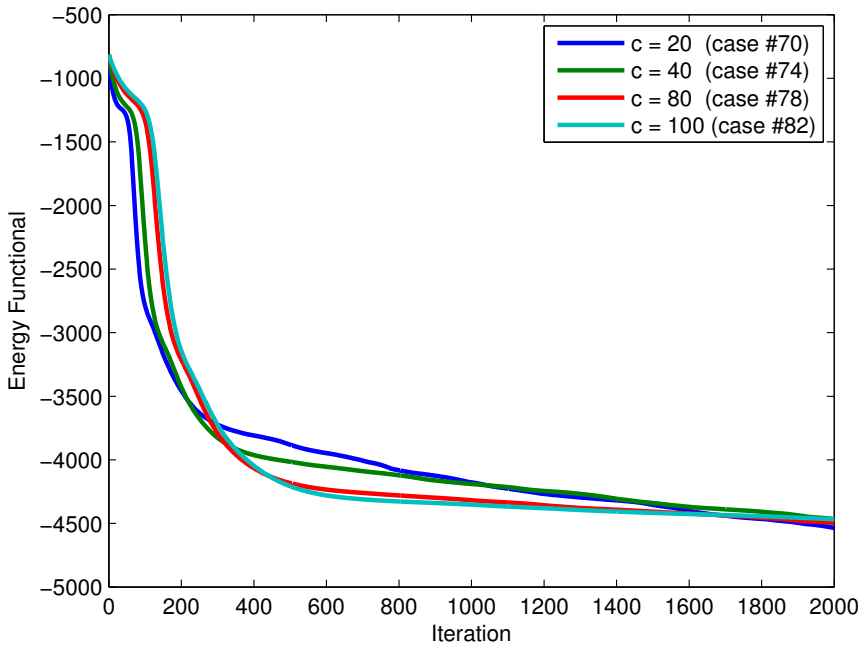

FIGURE 4. The variation of energy function with iteration for test cases #70, #74, #78 and #82 (τ is equal to 10 and c varies from 20 to 100).

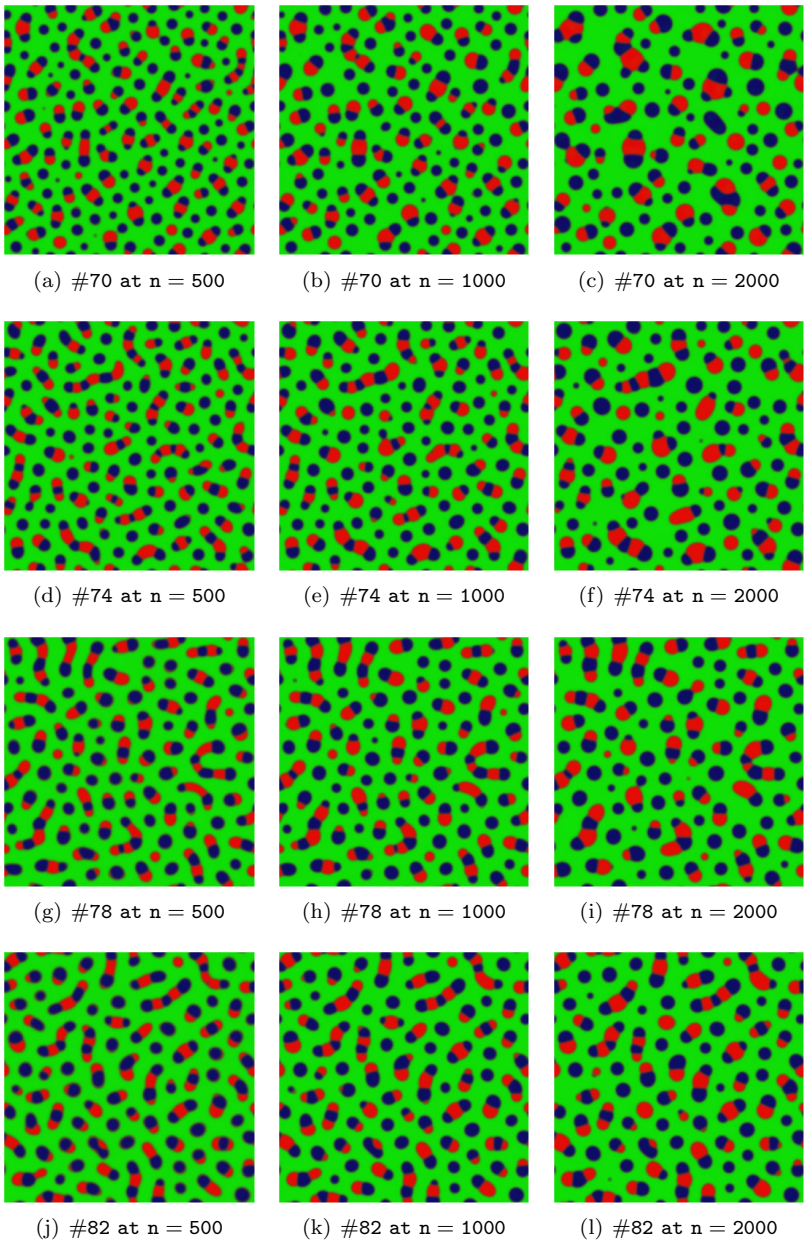

(a) #70 at n = 500 (b) #70 at n = 1000 (c) #70 at n = 2000

(d) #74 at n = 500 (e) #74 at n = 1000 (f) #74 at n = 2000

(g) #78 at n = 500 (h) #78 at n = 1000 (i) #78 at n = 2000

(j) #82 at n = 500 (k) #82 at n = 1000 (l) #82 at n = 2000

FIGURE 5. **u** at iterations 500, 1000 and 2000 for test cases #70, #74, #78 and #82.

Test cases #85-#114 are corresponding to modeling of spinodal decomposition in a four component system. In these cases, $\mathbf{F} = \mathbf{F_L}$ with $\theta = 0.25$, $\theta_c = 1$. Moreover, $p = 4$, $(\alpha, \beta) = (1, 0)$, $\varsigma = 0.05$, $(\Lambda_1, \Lambda_2, \Lambda_3, \Lambda_4) = (0.1, 0.1, 0.1, 0.7)$, $\zeta = 0$, $\texttt{nx} = 512$, $\texttt{iterm} = 2000$. The time stepsize and c respectively vary from 1 to 10^4 and 1 to 10 in these cases, as listed in table 5.

The energy functional values at the end of simulation (iteration 2000) are shown in table 6. Figure 6 shows the variation of energy functional with iteration for test cases #100-#104 ($c = 6$ and different values of τ). Similarly figure 7 shows the variation of energy functional with iteration for test cases #103, #108 and #113 ($\tau = 1000$ and different values of c). These plots demonstrate the convergence and energy stability of the presented algorithm. Figure 8 shows the distribution of phases at different iterations (times) for test cases #100-#104.

case	c	τ	case	c	τ	case	c	τ	case	c	τ	case	c	τ	case	c	τ
#85	1	10^0	#90	2	10^0	#95	4	10^0	#100	6	10^0	#105	8	10^0	#110	10	10^0
#86	1	10^1	#91	2	10^1	#96	4	10^1	#101	6	10^1	#106	8	10^1	#111	10	10^1
#87	1	10^2	#92	2	10^2	#97	4	10^2	#102	6	10^2	#107	8	10^2	#112	10	10^2
#88	1	10^3	#93	2	10^3	#98	4	10^3	#103	6	10^3	#108	8	10^3	#113	10	10^3
#89	1	10^4	#94	2	10^4	#99	4	10^4	#104	6	10^4	#109	8	10^4	#114	10	10^4

TABLE 5. The values of τ and c in test cases #85-#114.

case	$\mathbf{E}$	case	$\mathbf{E}$	case	$\mathbf{E}$	case	$\mathbf{E}$	case	$\mathbf{E}$	case	$\mathbf{E}$
#85	NaN	#90	1547	#95	1617	#100	1662	#105	1661	#110	1653
#86	NaN	#91	NaN	#96	NaN	#101	−1010	#106	−956	#111	−839
#87	NaN	#92	NaN	#97	NaN	#102	−1913	#107	−1829	#112	−1733
#88	NaN	#93	NaN	#98	NaN	#103	−2372	#108	−2413	#113	−2161
#89	NaN	#94	NaN	#99	NaN	#104	−2567	#109	−2484	#114	−2405

TABLE 6. The energy functional values at iteration 2000 for test cases #85-#114.

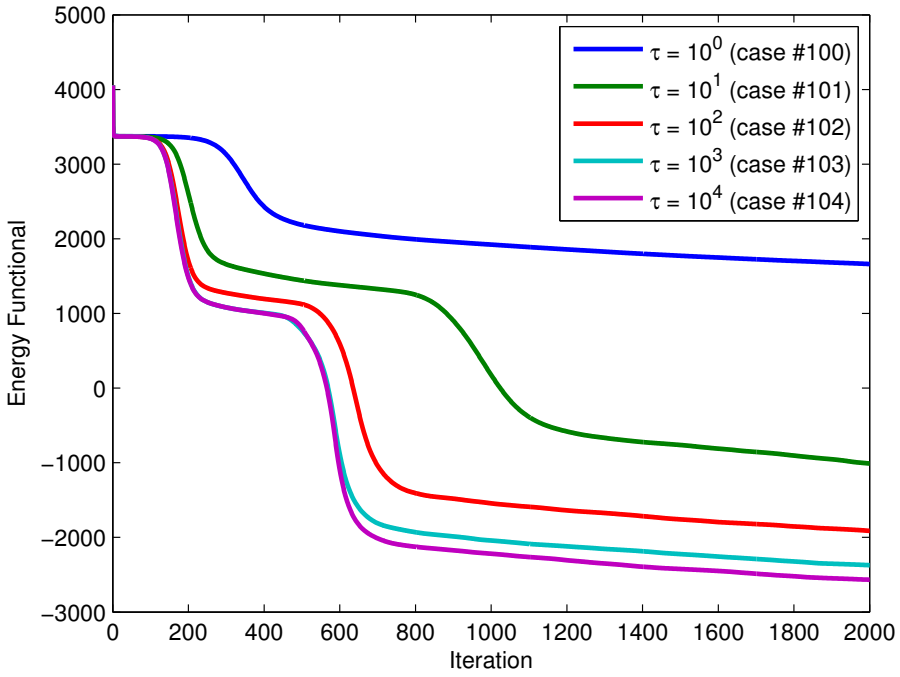

FIGURE 6. The variation of energy function with iteration for test cases #100-#104 (c is equal to 6 and τ varies from 1 to 10^4).

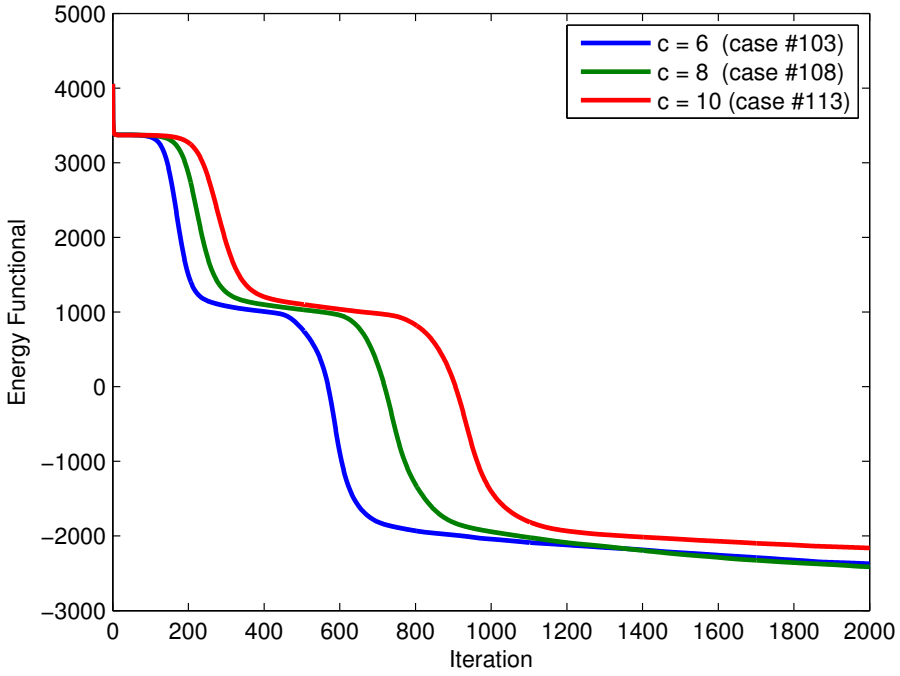

FIGURE 7. The variation of energy function with iteration for test cases #103, #108 and #113 (τ is equal to 1000 and c varies from 6 to 10).

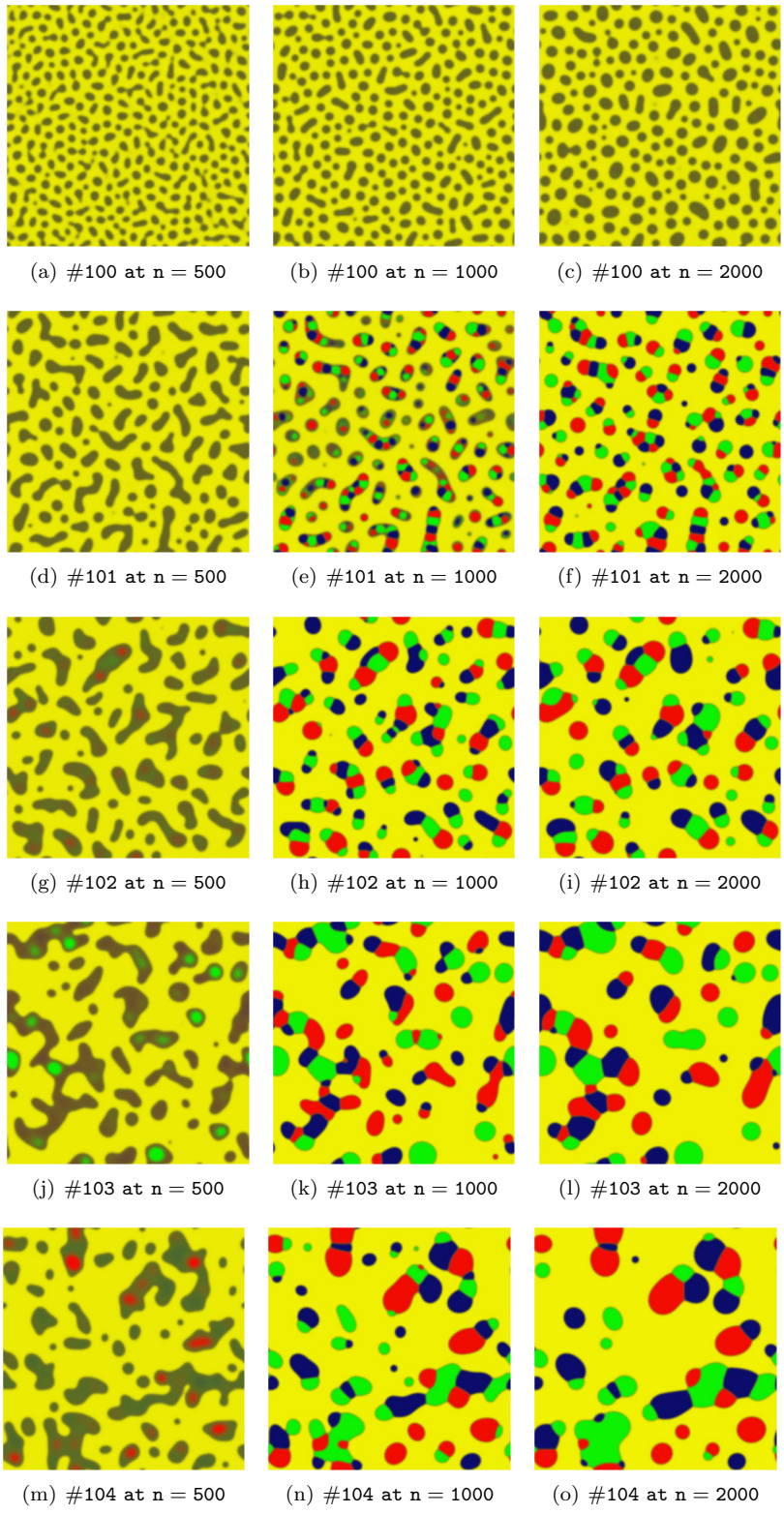

(a) #100 at n = 500 (b) #100 at n = 1000 (c) #100 at n = 2000

(d) #101 at n = 500 (e) #101 at n = 1000 (f) #101 at n = 2000

(g) #102 at n = 500 (h) #102 at n = 1000 (i) #102 at n = 2000

(j) #103 at n = 500 (k) #103 at n = 1000 (l) #103 at n = 2000

(m) #104 at n = 500 (n) #104 at n = 1000 (o) #104 at n = 2000

FIGURE 8. **u** at iterations 500, 1000 and 2000 for test cases #100-#104.

Test cases #115-#138 are corresponding to the approximate solution of the least perimeter periodic space tessellation with three equal partitions. In these cases, $\mathbf{F} = \mathbf{F_W}$, $p = 3$, $(\alpha, \beta) = (1, 0)$, $\varsigma = 10^{-8}$, $(\Lambda_1, \Lambda_2, \Lambda_3) = (1/3, 1/3, 1/3)$, $\zeta = 0$, $\mathtt{nx} = 128$, $\mathtt{iterm} = 2000$. The time stepsize and c respectively vary from 10^2 to 10^8 and 0.25 to 2 in these cases, as listed in table 7.

The energy functional values at the end of simulation (iteration 2000) are shown in table 8. The evolution of solution with iteration (time) for test cases #121 and #138 are shown in figure 9. Considering the least attained value of energy functional (see table 8) and figure 9, the lamellar microstructure appears to be the global minimizer of least perimeter periodic tessellation of 2D space with three equal area partitions. As formerly mentioned, every test case is run 5 times here and for each case the simulation with the least energy function at iteration 2000 is reported in table 8. To make sense about the topology of possible local solutions, some topologically different solutions at iterations 2000 and their corresponding energy function values are shown in figure 10 (these cases are chosen from 120 different simulations that are run for this example in the present study).

case	c	τ	case	c	τ	case	c	τ	case	c	τ	case	c	τ	case	c	τ
#115	0.25	10^2	#119	0.5	10^2	#123	0.75	10^2	#127	1	10^2	#131	1.5	10^2	#135	2	10^2
#116	0.25	10^4	#120	0.5	10^4	#124	0.75	10^4	#128	1	10^4	#132	1.5	10^4	#136	2	10^4
#117	0.25	10^6	#121	0.5	10^6	#125	0.75	10^6	#129	1	10^6	#133	1.5	10^6	#137	2	10^6
#118	0.25	10^8	#122	0.5	10^8	#126	0.75	10^8	#130	1	10^8	#134	1.5	10^8	#138	2	10^8

TABLE 7. The values of τ and c in test cases #115-#138.

case	**E**	case	**E**	case	**E**	case	**E**	case	**E**	case	**E**
#115	95.00	#119	95.07	#123	99.31	#127	98.70	#131	112.71	#135	105.68
#116	95.36	#120	94.68	#124	95.18	#128	94.71	#132	94.87	#136	96.57
#117	94.77	#121	93.41	#125	95.00	#129	94.70	#133	95.06	#137	89.05
#118	95.36	#122	95.10	#126	93.79	#130	94.44	#134	93.89	#138	87.54

TABLE 8. The energy functional values at iteration 2000 for test cases #115-#138.

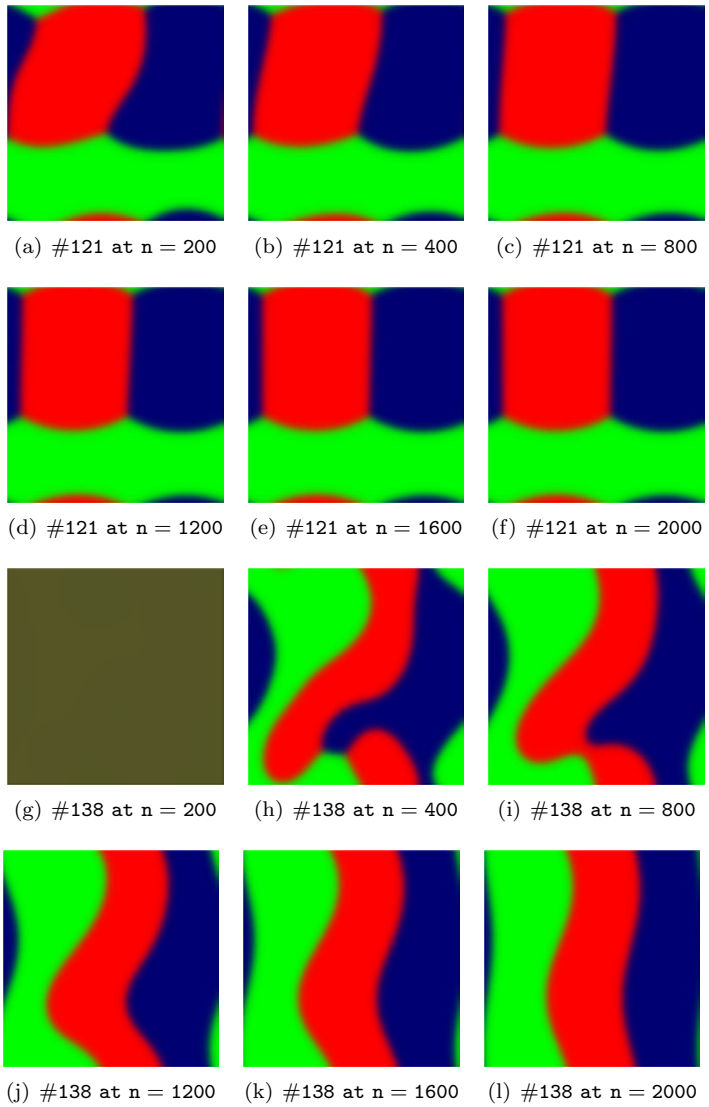

(a) #121 at n = 200 (b) #121 at n = 400 (c) #121 at n = 800

(d) #121 at n = 1200 (e) #121 at n = 1600 (f) #121 at n = 2000

(g) #138 at n = 200 (h) #138 at n = 400 (i) #138 at n = 800

(j) #138 at n = 1200 (k) #138 at n = 1600 (l) #138 at n = 2000

FIGURE 9. **u** at different iterations for test cases #121 and #138.

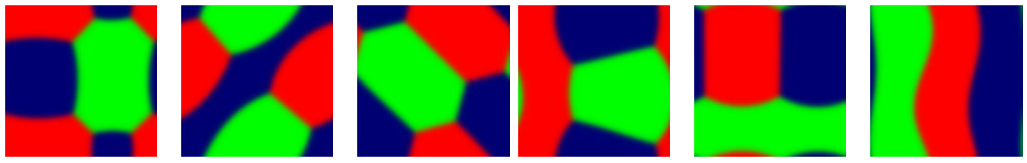

(a) $\mathbf{E} = 107.94$ (b) $\mathbf{E} = 107.61$ (c) $\mathbf{E} = 96.88$ (d) $\mathbf{E} = 94.70$ (e) $\mathbf{E} = 93.41$ (f) $\mathbf{E} = 87.54$

FIGURE 10. **u** and **E** at iteration 2000 for some selected test cases from cases #115-#138.

Test cases #139-#162 are corresponding to the approximate solution of least perimeter periodic tessellation of space with four equal area partitions. It is well known that the regular honeycomb microstructure is the global solution of this problem (c.f. [35, 61]). In these cases, $\mathbf{F} = \mathbf{F_W}$, $p = 4$, $(\alpha, \beta) = (1, 0)$, $\varsigma = 10^{-8}$, $(\Lambda_1, \Lambda_2, \Lambda_3, \Lambda_4) = (0.25, 0.25, 0.25, 0.25)$, $\zeta = 0$, $\texttt{nx} = 128$, $\texttt{iterm} = 4000$. τ and c respectively vary from 10^2 to 10^8 and 0.25 to 2 in these cases, as listed in table 9.

The energy functional values at the end of simulation (iteration 4000) are shown in table 10. In all cases algorithm is successful and the $\mathbf{E}$ decreased monotonically with iteration (time). As an example, figure 11 shows the variation of $\mathbf{E}$ with iteration for test case #139. The evolution of solution with iteration (time) for test cases #139 is shown in figure 12. Figure 13 shows $\mathbf{u}$ at iteration 4000 (final solution) for test cases #139-#162. According to the plots, except in cases #153 and #155, the algorithm found the outline of global solution after 4000 time steps. To make sense about possible local solutions of this problem, $\mathbf{u}$ at iteration 4000 is plotted in figure 14 for some topologically different solutions resulted by the presented algorithm.

case	c	τ	case	c	τ	case	c	τ	case	c	τ	case	c	τ	case	c	τ
#139	0.25	10^2	#143	0.5	10^2	#147	0.75	10^2	#151	1	10^2	#155	1.5	10^2	#159	2	10^2
#140	0.25	10^4	#144	0.5	10^4	#148	0.75	10^4	#152	1	10^4	#156	1.5	10^4	#160	2	10^4
#141	0.25	10^6	#145	0.5	10^6	#149	0.75	10^6	#153	1	10^6	#157	1.5	10^6	#161	2	10^6
#142	0.25	10^8	#146	0.5	10^8	#150	0.75	10^8	#154	1	10^8	#158	1.5	10^8	#162	2	10^8

TABLE 9. The values of τ and c in test cases #139-#162.

case	$\mathbf{E}$	case	$\mathbf{E}$	case	$\mathbf{E}$	case	$\mathbf{E}$	case	$\mathbf{E}$	case	$\mathbf{E}$
#139	105.35	#143	106.67	#147	109.05	#151	108.59	#155	116.22	#159	110.48
#140	107.41	#144	107.48	#148	106.45	#152	108.50	#156	108.83	#160	107.79
#141	108.30	#145	108.82	#149	108.82	#153	112.84	#157	108.87	#161	108.96
#142	108.82	#146	107.41	#150	105.61	#154	108.84	#158	107.60	#162	107.90

TABLE 10. The energy functional values at iteration 4000 for test cases #139-#162.

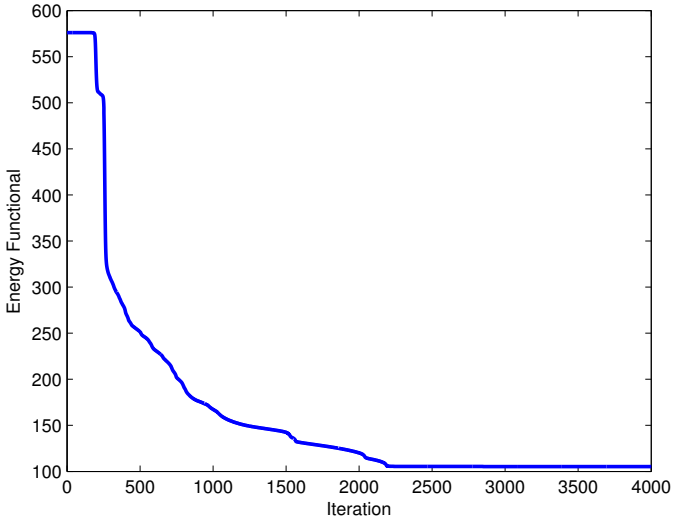

FIGURE 11. The variation of energy functional with iteration for test case #139.

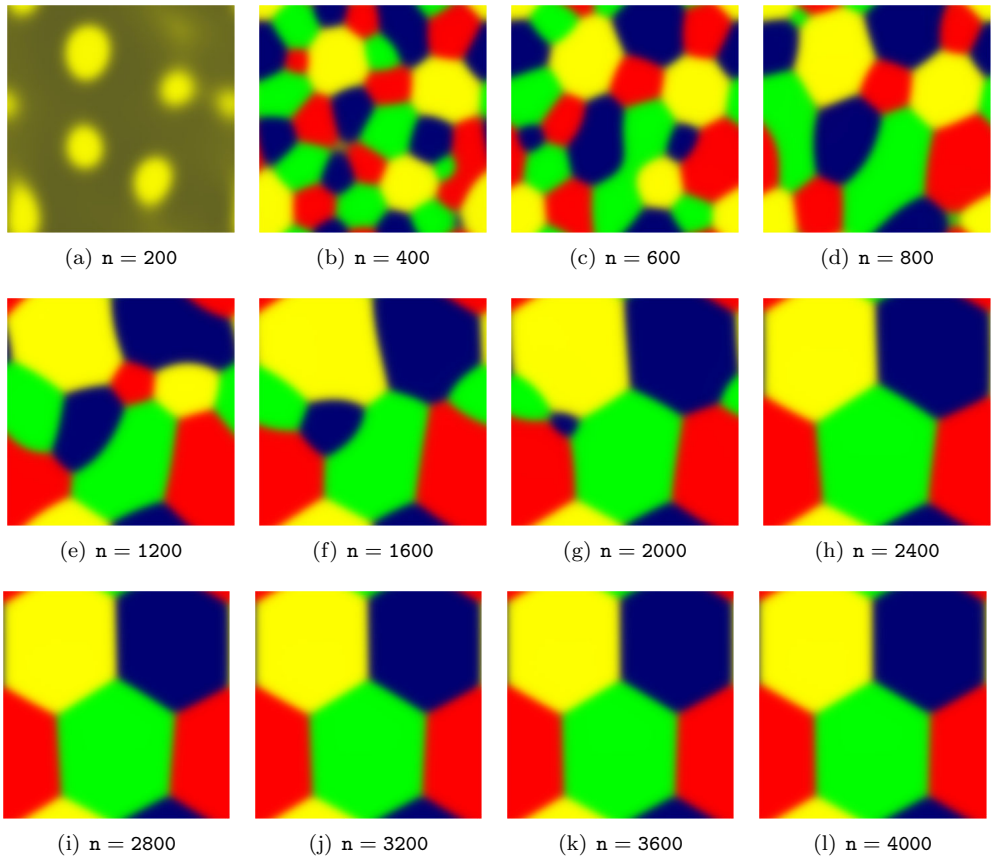

(a) $\mathtt{n} = 200$ (b) $\mathtt{n} = 400$ (c) $\mathtt{n} = 600$ (d) $\mathtt{n} = 800$

(e) $\mathtt{n} = 1200$ (f) $\mathtt{n} = 1600$ (g) $\mathtt{n} = 2000$ (h) $\mathtt{n} = 2400$

(i) $\mathtt{n} = 2800$ (j) $\mathtt{n} = 3200$ (k) $\mathtt{n} = 3600$ (l) $\mathtt{n} = 4000$

FIGURE 12. The evolution of $\mathbf{u}$ with iteration (time) for test case #139.

Test cases #163 and #164 are corresponding to the approximate solution of the least perimeter periodic tessellation of space with 8 and 16 equal partitions respectively. Obviously, the global minimizer of these problems are again the honeycomb microstructure. In these test problems $\mathbf{F} = \mathbf{F}_{\mathbf{W}}$, $p = 8, 16$, $(\alpha, \beta) = (1, 0)$, $\varsigma = 10^{-8}$, $\Lambda_i = 1/p$ (for $i = 1, \ldots, p$), $\mathtt{nx} = 256$, $\tau = 10^3$, $c = 1$, $\mathtt{iterm} = 20000$. Unlike test cases #115-#162, when $\zeta = 0$, the separation of phases does not happen in cases #163 and #164, when we start from a randomly perturbed uniform concentration field (even when the amplitude of perturbation is sufficiently large). In these conditions, solutions converge to the uniform concentration fields. To cope this problem, the penalization strategy developed in section 4 is used here. For this purpose, the nonzero value 1000 is used for the penalization parameter ζ in these problems. As a general rule, ζ should be chosen such that the values of $\zeta P(\mathbf{u})$ and $\mathbf{E}(\mathbf{u})$ will be comparable at the start of simulation (for instance $\zeta \approx 0.2\, \mathbf{E}(\mathbf{u})/P(\mathbf{u})$ is a good choice according to our numerical experiments).

The variation of energy functional with iteration is shown in figures 15 and 16. The evolution of solutions with iteration (time) are shown in figures 17 and 18 for test cases #163 and #164 respectively. According to the plots the algorithm is convergent and energy stable. Furthermore, the distribution of phases converge to honeycomb microstructure as it is expected by theory. This observation confirms the success of presented penalization strategy to avoid the trivial solution.

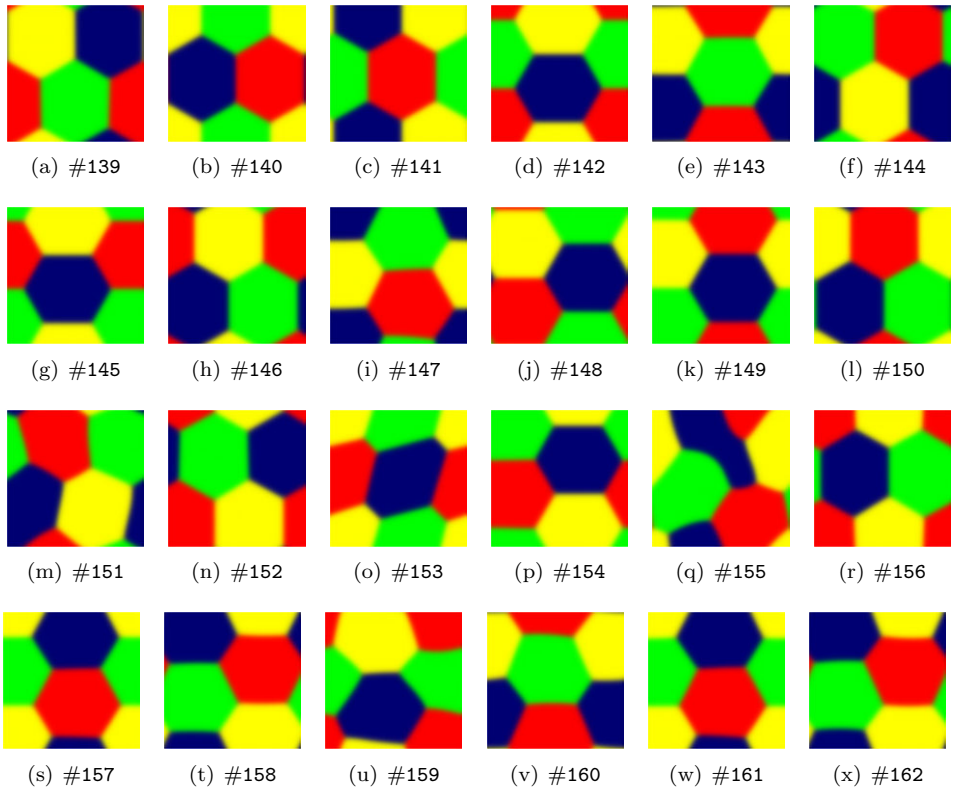

(a) #139 (b) #140 (c) #141 (d) #142 (e) #143 (f) #144

(g) #145 (h) #146 (i) #147 (j) #148 (k) #149 (l) #150

(m) #151 (n) #152 (o) #153 (p) #154 (q) #155 (r) #156

(s) #157 (t) #158 (u) #159 (v) #160 (w) #161 (x) #162

FIGURE 13. **u** at iteration 4000 for test case #139-#162.

(a) $\mathbf{E} = 105.3$ (b) $\mathbf{E} = 110.4$ (c) $\mathbf{E} = 110.8$ (d) $\mathbf{E} = 113.4$ (e) $\mathbf{E} = 113.4$ (f) $\mathbf{E} = 119.9$ (g) $\mathbf{E} = 126.9$

FIGURE 14. **u** and **E** at iteration 4000 for some selected test cases from cases #139-#162.

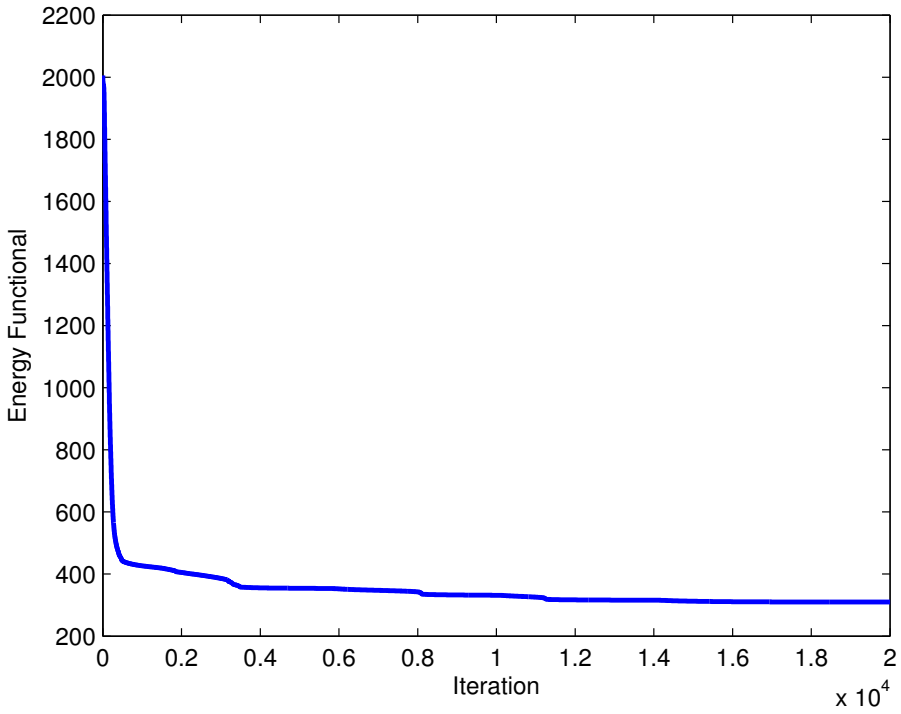

FIGURE 15. The variation of energy function with iteration (time) for test case #163.

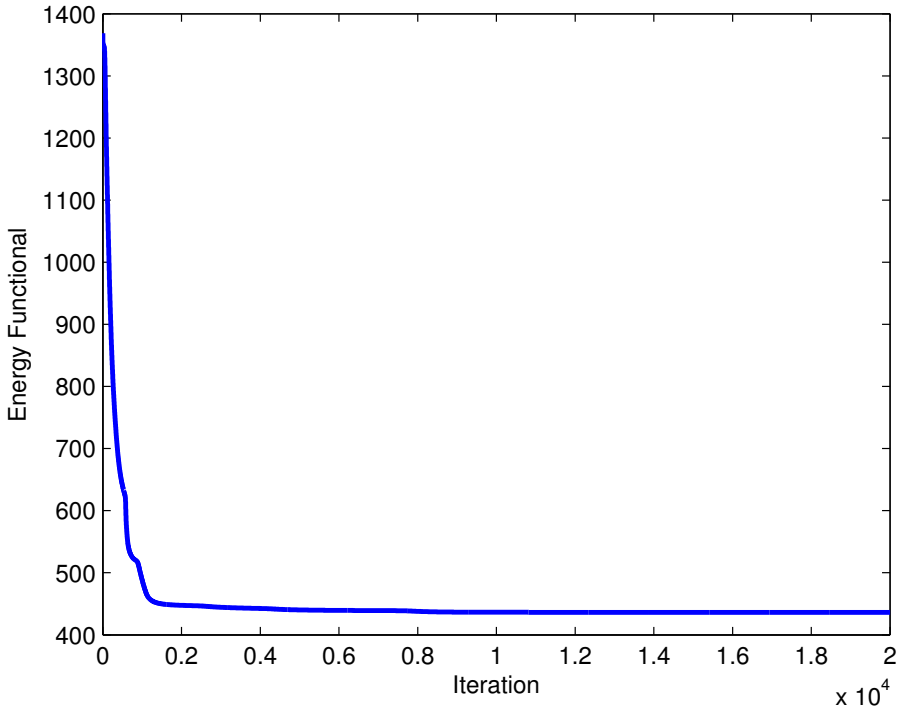

FIGURE 16. The variation of energy function with iteration (time) for test case #164.

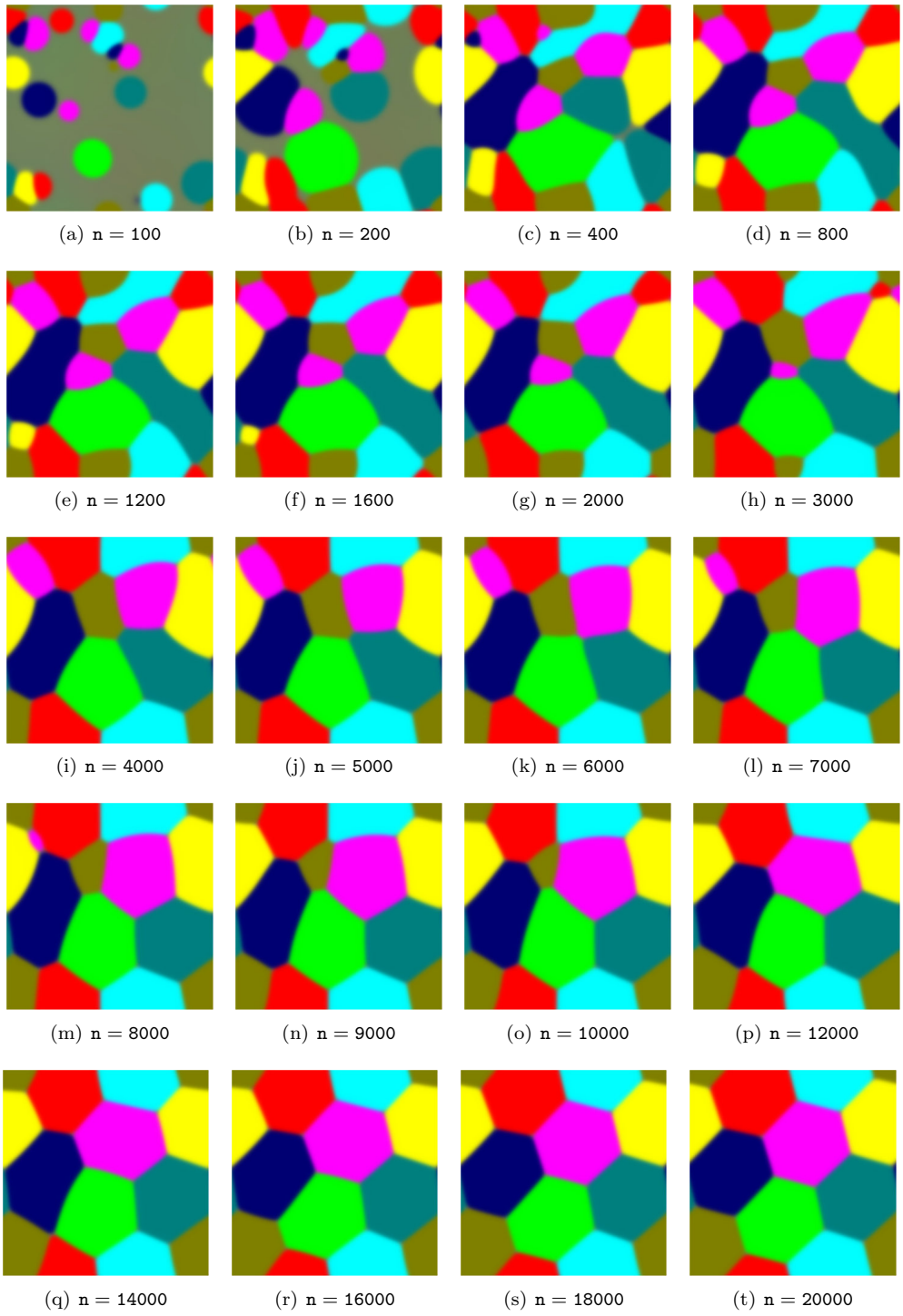

(a) n = 100 (b) n = 200 (c) n = 400 (d) n = 800

(e) n = 1200 (f) n = 1600 (g) n = 2000 (h) n = 3000

(i) n = 4000 (j) n = 5000 (k) n = 6000 (l) n = 7000

(m) n = 8000 (n) n = 9000 (o) n = 10000 (p) n = 12000

(q) n = 14000 (r) n = 16000 (s) n = 18000 (t) n = 20000

FIGURE 17. The evolution of **u** with iteration (time) for test case #163.

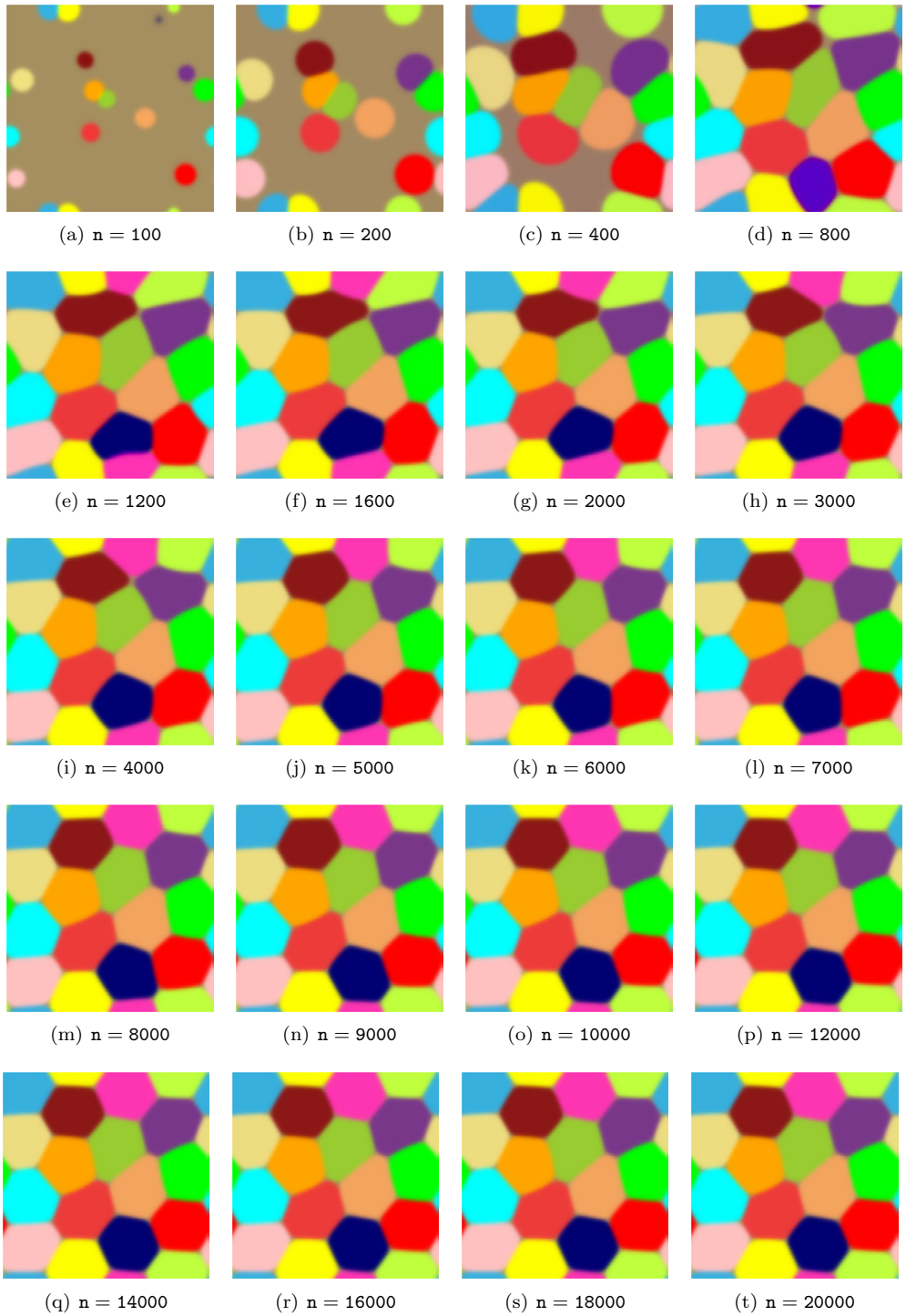

(a) n = 100 (b) n = 200 (c) n = 400 (d) n = 800

(e) n = 1200 (f) n = 1600 (g) n = 2000 (h) n = 3000

(i) n = 4000 (j) n = 5000 (k) n = 6000 (l) n = 7000

(m) n = 8000 (n) n = 9000 (o) n = 10000 (p) n = 12000

(q) n = 14000 (r) n = 16000 (s) n = 18000 (t) n = 20000

FIGURE 18. The evolution of **u** with iteration (time) for test case #164.

Finally, table 11 shows the CPU times corresponding to test cases #1, #61, #85, #115, #139, #163 and #164. These values are corresponding to the typical CPU times for test cases #1-#60, #61-#84, #85-#114, #115-#138, #139-#162, #163 and #164 respectively.

case	**CPU**	case	**CPU**	case	**CPU**	case	**CPU**	case	**CPU**	case	**CPU**	case	**CPU**
#1	702	#61	773	#85	957	#115	39	#139	128	#163	6709	#164	14762

TABLE 11. The CPU time (in second) corresponding to some selected test cases.

6. Conclusion and future outlook

An unconditionally energy stable algorithm is introduced to solve Cahn-Morral-like equations in the present study. This algorithm uses the Eyre's convex-concave splitting time stepping scheme to avoid time stepsize restriction due to the stability of numerical solution and Schur complement method to maintain the feasibility of solution with respect to pointwise incompressibility constraints at every time step. By an appropriate selection of splitting parameter, the method is convergent and unconditionally energy stable. The algorithm is applied to model the spinodal decomposition in multicomponent systems and optimal space partitioning problem. A penalization strategy is suggested for the later kind of problem to avoid the trivial solution. The success of presented algorithm is demonstrated by means of extensive numerical experiments including 164 test problems. According to our numerical results, using a large time stepsize does not essentially lead to the best computational performance. However, there is an effective time stepsize for every selection of splitting parameter such that there are optimal choices for the binary time stepsize and splitting parameter.

The theoretical analysis of the presented algorithm to prove its unconditional energy stability and to find hints for choosing optimal values of time stepsize and splitting parameter is suggested as outline of future researches. Furthermore, the introduced method in this paper can be straightforwardly extended to solve alternative multi phase-field problems, like vector-valued Allen-Cahn equation, multi phase-field crystal equation, etc. Extension of this algorithm to solve these kinds of problems can be considered as the scope of future studies.

Acknowledgment

We would like to thank Edouard Oudet for his helpful comments in the course of this work.

Appendix A. MATLAB codes

MATLAB script to solve the Cahn-Morral equation with logarithmic free energy density

```
clear all; clc;
p = 3; nx = 256; alpha = 1; beta = 0; c = 3; tau = 100; iterm = 500;
eps = 1; theta = 0.3; theta_c = 1; amp = 0.05; v = [0.15 0.2 0.65];

k = [0:nx/2 -nx/2+1:-1]*(2*pi/nx);
[kx,ky] = meshgrid(k,k);
L = -(kx.^2 + ky.^2); L2 = L.*L;
...
u = zeros(nx,nx,p);
U = complex(zeros(nx,nx,p),zeros(nx,nx,p));
for j = 1:p-1
 u(:,:,j) = v(j) + amp*(2*rand(nx,nx)-1);
 U(:,:,j) = fft2(u(:,:,j));
end
u(:,:,p) = 1 - sum(u(:,:,1:p-1),3);
U(:,:,p) = fft2(u(:,:,p));
R = complex(zeros(nx,nx,p-1),zeros(nx,nx,p-1));
ONE_hat = fft2(ones(nx,nx));

for iter = 1:iterm
 ...
 i = 1:nx-1; j = 1:nx-1; ip = i+1; jp = j+1;
 E1 = (u(ip,j,:)-u(i,j,:)).^2 + (u(i,jp,:)-u(i,j,:)).^2;
 E2 = u.*log(u);
 E3 = zeros(nx,nx);
 for i = 1:p
  for j = i+1:p
  E3 = E3 + u(:,:,i).*u(:,:,j);
  end
 end
 E = (eps/2)*sum(E1(:)) + theta*sum(E2(:)) + theta_c*sum(E3(:));
 fprintf('Iter : %6i E(u) : %11.5f\n', iter, E);

 if mod(iter,50) == 0
  colors = [1 0 0; 0 0 1; 0 1 0; 1 1 0];
  uu = reshape(u,nx*nx,p)*colors(1:p,:);
  img = imresize(reshape(min(max(uu,0),1),nx,nx,3),10,'bilinear');
  image(img), axis image off, drawnow;
 end
end
```

MATLAB script to solve the Cahn-Morral equation with multi-well polynomical free energy density

```
clear all; clc;
p = 4; nx = 128; c = 0.25; tau = 100; zeta = 100; iterm = 4000;
eps = 1; amp = 1.e-8; v = [0.25 0.25 0.25 0.25];

k = [0:nx/2 -nx/2+1:-1]*(2*pi/nx);
[kx,ky] = meshgrid(k,k);
L = -(kx.^2 + ky.^2); L2 = L.*L;
...
sigma_exact = sqrt(v.*(1-v));
u = zeros(nx,nx,p); gs = zeros(nx,nx,p);
U = complex(zeros(nx,nx,p),zeros(nx,nx,p));
for j = 1:p-1
 u(:,:,j) = v(j) + amp*(2*rand(nx,nx)-1);
 U(:,:,j) = fft2(u(:,:,j));
end
u(:,:,p) = 1 - sum(u(:,:,1:p-1),3);
U(:,:,p) = fft2(u(:,:,p));
R = complex(zeros(nx,nx,p-1),zeros(nx,nx,p-1));
ONE_hat = fft2(ones(nx,nx));

for iter = 1:iterm
 ...

 i = 1:nx-1; j = 1:nx-1; ip = i+1; jp = j+1;
 E1 = (u(ip,j,:)-u(i,j,:)).^2 + (u(i,jp,:)-u(i,j,:)).^2;
 E2 = (u.^2).*((u - 1).^2);
 E3 = 0;
 for j = 1:p
  uj = u(:,:,j); uj = uj(:); sigma_j = sqrt(mean((uj - v(j)).^2));
  E3 = E3 + 0.5*(sigma_j - sigma_exact(j))^2;
 end
 E = (eps/2)*sum(E1(:)) + (0.25)*sum(E2(:)) + zeta*E3;
 fprintf('Iter : %6i E(u) : %11.5f\n',iter, E);

 if mod(iter,200) == 0
  colors = [1 0 0; 0 0 1; 0 1 0; 1 1 0];
  img = imresize(reshape(min(max(reshape(u,nx*nx,p)*colors(1:p,:),0),1),nx,nx,3),10,'bilinear');
  image(img), axis image off, drawnow;
 end
end
```

References

[1] S. Baldo. Minimal interface criterion for phase transitions in mixtures of cahn-hilliard fluids. *Ann Inst H. Poincaré (C) Anal Non Linéaire*, 7(2):67–90, 1990.

[2] J.W. Barrett and J.F. Blowey. An error bound for the finite element approximation of a model for phase separation of a multi-component alloy. *IMA J Numer Anal*, 16(2):257–287, 1996.

[3] J.W. Barrett and J.F. Blowey. Finite element approximation of a model for phase separation of a multi-component alloy with non-smooth free energy. *Numer Math*, 77(1):1–34, 1997.

[4] J.W. Barrett and J.F. Blowey. Finite element approximation of a model for phase separation of a multi-component alloy with a concentration-dependent mobility matrix. *IMA J Numer Anal*, 18(2):287–328, 1998.

[5] J.W. Barrett and J.F. Blowey. An improved error bound for a finite element approximation of a model for phase separation of a multi-component alloy with a concentration dependent mobility matrix. *Numer Math*, 88(2):255–297, 2001.

[6] J.W. Barrett, J.F. Blowey, and H. Garcke. On fully practical finite element approximations of degenerate cahn-hilliard systems. *ESAIM: Math Mod Numer Anal*, 35(04):713–748, 2001.

[7] A.L. Bertozzi, S. Esedoglu, and A. Gillette. Inpainting of binary images using the cahn-hilliard equation. *IEEE Transa image processing*, 16(1):285–291, 2007.

[8] S. Bhattacharyya and T.A. Abinandanan. A study of phase separation in ternary alloys. *Bul Mater Sci*, 26(1):193–197, 2003.
[9] L. Blank, L. Sarbu, and M. Stoll. Preconditioning for allen–cahn variational inequalities with non-local constraints. *J Comput Phys*, 231(16):5406–5420, 2012.
[10] J.F. Blowey, M.I.M. Copetti, and C.M. Elliott. Numerical analysis of a model for phase separation of a multicomponent alloy. *IMA J Numer Anal*, 16(1):111–139, 1996.
[11] J. Bosch, M. Stoll, and P. Benner. Fast solution of cahn–hilliard variational inequalities using implicit time discretization and finite elements. *J Comput Phys*, 262:38–57, 2014.
[12] P. Boyanova and M. Neytcheva. Efficient numerical solution of discrete multi-component cahn–hilliard systems. *Comput Math Appl*, 67(1):106–121, 2014.
[13] F. Boyer and S. Minjeaud. Numerical schemes for a three component cahn-hilliard model. *ESAIM: Math Mod Numer Anal*, 45(04):697–738, 2011.
[14] J. Cahn. On spinodal decomposition. *Acta Metal*, 9(9):795–801, 1961.
[15] J. Cahn and J. Hilliard. Spinodal decomposition: A reprise. *Acta Metal*, 19(2):151–161, 1971.
[16] J.W. Cahn and J.E. Hilliard. Free energy of a nonuniform system. i. interfacial free energy. *J Chem Phys*, 28(2):258–267, 1958.
[17] F. Chen and J. Shen. Efficient energy stable schemes with spectral discretization in space for anisotropic cahn-hilliard systems. *Commun. Comput. Phys*, 13:1189–1208, 2013.
[18] L. Chen. Computer simulation of spinodal decomposition in ternary systems. *Acta Metal*, 42(10):3503–3513, 1994.
[19] M. Cheng and J.A. Warren. An efficient algorithm for solving the phase field crystal model. *J Comput Phys*, 227(12):6241–6248, 2008.
[20] M.I.M. Copetti. Numerical experiments of phase separation in ternary mixtures. *Math Comput Sim*, 52(1):41–51, 2000.
[21] S.J. Cox and E. Flikkema. The minimal perimeter for n confined deformable bubbles of equal area. *Electron J Combinatorics*, 17(1):R45, 2010.
[22] S.M. Cox and P.C. Matthews. Exponential time differencing for stiff systems. *J Comput Phys*, 176(2):430–455, 2002.
[23] L. Cueto-Felgueroso and J. Peraire. A time-adaptive finite volume method for the cahn–hilliard and kuramoto–sivashinsky equations. *J Comput Phys*, 227(24):9985–10017, 2008.
[24] D. De Fontaine. *A computer simulation of the evolution of coherent composition variations in solid solutions*. PhD thesis, Northwestern University, 1967.
[25] D. De Fontaine. An analysis of clustering and ordering in multicomponent solid solutionsi. stability criteria. *J Phys Chem Solids*, 33(2):297–310, 1972.
[26] D. De Fontaine. An analysis of clustering and ordering in multicomponent solid solutionsii fluctuations and kinetics. *J Phys Chem Solids*, 34(8):1285–1304, 1973.
[27] E.V.L. De Mello and Otton T. da Silveira F. Numerical study of the cahn–hilliard equation in one, two and three dimensions. *Physica A*, 347:429–443, 2005.
[28] J.P. Desi, H.H. Edrees, J.J. Price, E. Sander, and T. Wanner. The dynamics of nucleation in stochastic cahn-morral systems. *SIAM J Appl Dyn Sys*, 10(2):707–743, 2011.
[29] C.M. Elliott and S. Luckhaus. A generalised diffusion equation for phase separation of a multi-component mixture with interfacial free energy. *IMA Preprint Series 887*, 1991.
[30] M. Elsey and B. Wirth. A simple and efficient scheme for phase field crystal simulation. *ESAIM: Math Model Numer Anal*, 47(05):1413–1432, 2013.
[31] D. Eyre. An unconditionally stable one-step scheme for gradient systems. *preprint*, 1997.
[32] D.J. Eyre. Systems of cahn-hilliard equations. *SIAM J Appl Math*, 53(6):1686–1712, 1993.
[33] D.J. Eyre. Unconditionally gradient stable time marching the cahn-hilliard equation. In *MRS Proceedings*, volume 529, page 39. Cambridge Univ Press, 1998.
[34] P.C. Fife. Models for phase separation and their mathematics. *Electron J Differ Equations*, 2000(48):1–26, 2000.
[35] H. Garcke, B. Nestler, B. Stinner, and F. Wendler. Allen–cahn systems with volume constraints. *Math Mod Meth Appl Sci*, 18(08):1347–1381, 2008.
[36] H. Gómez, V.M. Calo, Y. Bazilevs, and T. Hughes. Isogeometric analysis of the cahn–hilliard phase-field model. *Comput Meth Appl Mech Eng*, 197(49):4333–4352, 2008.
[37] H. Gomez and X. Nogueira. An unconditionally energy-stable method for the phase field crystal equation. *Comput Meth Appl Mech Eng*, 249:52–61, 2012.

[38] H. Gomez, A. Reali, and G. Sangalli. Accurate, efficient, and (iso) geometrically flexible collocation methods for phase-field models. *J Comput Phys*, 262:153–171, 2014.
[39] C. Gräser, R. Kornhuber, and U. Sack. Nonsmooth schur–newton methods for multicomponent cahn–hilliard systems. *IMA J Numer Anal, inpress*, 2014.
[40] Zhen Guan, John S Lowengrub, Cheng Wang, and Steven M Wise. Second order convex splitting schemes for periodic nonlocal cahn–hilliard and allen–cahn equations. *J Comput Phys*, 277:48–71, 2014.
[41] Zhen Guan, Cheng Wang, and Steven M Wise. A convergent convex splitting scheme for the periodic nonlocal cahn-hilliard equation. *Numerische Mathematik*, 128(2):377–406, 2014.
[42] F. Guillén-González and G. Tierra. On linear schemes for a cahn–hilliard diffuse interface model. *J Comput Phys*, 234:140–171, 2013.
[43] U. Hecht, L. Gránásy, T. Pusztai, B. Böttger, M. Apel, V. Witusiewicz, L. Ratke, J. DeWilde, L. Froyen, and D. Camel. Multiphase solidification in multicomponent alloys. *Mater Sci Eng R*, 46(1):1–49, 2004.
[44] M. Honjo and Y. Saito. Numerical simulation of phase separation in fe–cr binary and fe–cr–mo ternary alloys with use of the cahn–hilliard equation. *ISIJ International*, 40(9):914–919, 2000.
[45] J. Hoyt. The continuum theory of nucleation in multicomponent systems. *Acta Metal*, 38(8):1405–1412, 1990.
[46] J. Hoyt. Linear spinodal decomposition in a regular ternary alloy. *Acta Metal*, 38(2):227–231, 1990.
[47] Zhengzheng Hu, Steven M Wise, Cheng Wang, and John S Lowengrub. Stable and efficient finite-difference nonlinear-multigrid schemes for the phase field crystal equation. *J Comput Phys*, 228(15):5323–5339, 2009.
[48] A.K. Kassam and L.N. Trefethen. Fourth-order time-stepping for stiff pdes. *SIAM J Sci Comput*, 26(4):1214–1233, 2005.
[49] D. Kay and R. Welford. A multigrid finite element solver for the cahn–hilliard equation. *J Comput Phys*, 212(1):288–304, 2006.
[50] J. Kim, K. Kang, and J. Lowengrub. Conservative multigrid methods for cahn–hilliard fluids. *J Comput Phys*, 193(2):511–543, 2004.
[51] J.S. Kirkaldy. A ginzburg-landau treatment of ternary spinodal decomposition. *J Mater Sci*, 35(5):1177–1180, 2000.
[52] T. Kuwajima, Y. Saito, and Y. Suwa. Kinetics of phase separation in iron-based ternary alloys. ii. numerical simulation of phase separation in fe–cr–x (x= mo, cu) ternary alloys. *Intermetallics*, 11(11):1279–1285, 2003.
[53] A.G. Lamorgese, D. Molin, and R. Mauri. Phase field approach to multiphase flow modeling. *Milan J Math*, 79(2):597–642, 2011.
[54] D. Lee, J. Huh, D. Jeong, J. Shin, A. Yun, and J. Kim. Physical, mathematical, and numerical derivations of the cahn–hilliard equation. *Comput Mater Sci*, 81:216–225, 2014.
[55] H. Lee, J. Choi, and J. Kim. A practically unconditionally gradient stable scheme for the n-component cahn–hilliard system. *Physica A*, 391(4):1009–1019, 2012.
[56] H.G. Lee and J. Kim. A second-order accurate non-linear difference scheme for the n-component cahn–hilliard system. *Physica A*, 387(19):4787–4799, 2008.
[57] J. Liu, L. Dedè, J.A. Evans, M.J. Borden, and T. Hughes. Isogeometric analysis of the advective cahn–hilliard equation: spinodal decomposition under shear flow. *J Comput Phys*, 242:321–350, 2013.
[58] J. Morral and J. Cahn. Spinodal decomposition in ternary systems. *Acta Metal*, 19(10):1037–1045, 1971.
[59] B. Nestler and A. Choudhury. Phase-field modeling of multi-component systems. *Current Opinion Solid State Mater Sci*, 15(3):93–105, 2011.
[60] B. Nestler, F. Wendler, M. Selzer, B. Stinner, and H. Garcke. Phase-field model for multiphase systems with preserved volume fractions. *Phys Rev E*, 78(1):011604, 2008.
[61] E. Oudet. Approximation of partitions of least perimeter by γ-convergence: around kelvins conjecture. *Exp Math*, 20(3):260–270, 2011.
[62] N. Provatas and K. Elder. *Phase-field methods in materials science and engineering*. John Wiley & Sons, 2010.
[63] Z. Qiao, Z. Sun, and Z. Zhang. Stability and convergence of second-order schemes for the nonlinear epitaxial growth model without slope selection. *Math Comput*, 84(292):653–674, 2015.
[64] N. Raza, S. Sial, and A.R. Butt. Numerical approximation of time evolution related to ginzburg–landau functionals using weighted sobolev gradients. *Comput Math Appl*, 67(1):210–216, 2014.
[65] N. Raza, S. Sial, and S. Siddiqi. Approximating time evolution related to ginzburg–landau functionals via sobolev gradient methods in a finite-element setting. *J Comput Phys*, 229(5):1621–1625, 2010.

[66] N. Raza, S. Sial, and S.S. Siddiqi. Sobolev gradient approach for the time evolution related to energy minimization of ginzburg–landau functionals. *J Comput Phys*, 228(7):2566–2571, 2009.
[67] Y. Saad. *Iterative methods for sparse linear systems*. SIAM, 2003.
[68] C. Schönlieb and A. Bertozzi. Unconditionally stable schemes for higher order inpainting. *Commun Math Sci*, 9(2):413–457, 2011.
[69] J. Shen, C. Wang, X. Wang, and S.M. Wise. Second-order convex splitting schemes for gradient flows with ehrlich-schwoebel type energy: application to thin film epitaxy. *SIAM J Numer Anal*, 50(1):105–125, 2012.
[70] J. Shen and X. Yang. Numerical approximations of allen-cahn and cahn-hilliard equations. *Discrete Continuous Dynamical. Syst. A*, 28:1669–1691, 2010.
[71] J. Shen, X. Yang, and H. Yu. Efficient energy stable numerical schemes for a phase field moving contact line model. *J Comput Phys*, 284:617–630, 2015.
[72] S. Sial, J. Neuberger, T. Lookman, and A. Saxena. Energy minimization using sobolev gradients: application to phase separation and ordering. *J Comput Phys*, 189(1):88–97, 2003.
[73] Irina Singer-Loginova and HM Singer. The phase field technique for modeling multiphase materials. *Reports Progress Phys*, 71(10):106501, 2008.
[74] R. Tavakoli. Multimaterial topology optimization by volume constrained allen–cahn system and regularized projected steepest descent method. *Comput Meth Appl Mech Eng*, 276:534–565, 2014.
[75] R. Tavakoli. Computationally efficient approach for the minimization of volume constrained vector-valued ginzburg-landau energy functional. *J Comput Phys*, 295:355–378, 2015.
[76] R. Tavakoli and S.M. Mohseni. Alternating active-phase algorithm for multimaterial topology optimization problems: a 115-line matlab implementation. *Struct Multidisc Optim*, 49(4):621–642, 2014.
[77] G. Tierra and F. Guillén-González. Numerical methods for solving the cahn–hilliard equation and its applicability to related energy-based models. *Arch Comput Meth Eng*, pages 1–21, 2014.
[78] Lloyd N Trefethen. *Spectral methods in MATLAB*, volume 10. SIAM, 2000.
[79] B.P. Vollmayr-Lee and A.D. Rutenberg. Fast and accurate coarsening simulation with an unconditionally stable time step. *Phys Rev E*, 68(6):066703, 2003.
[80] S. Wise, J. Kim, and J. Lowengrub. Solving the regularized, strongly anisotropic cahn–hilliard equation by an adaptive nonlinear multigrid method. *J Comput Phys*, 226(1):414–446, 2007.
[81] S.M. Wise, C. Wang, and J.S. Lowengrub. An energy-stable and convergent finite-difference scheme for the phase field crystal equation. *SIAM J Numer Anal*, 47(3):2269–2288, 2009.
[82] O. Wodo and B. Ganapathysubramanian. Computationally efficient solution to the cahn–hilliard equation: Adaptive implicit time schemes, mesh sensitivity analysis and the 3d isoperimetric problem. *J Comput Phys*, 230(15):6037–6060, 2011.
[83] L. Zhang, M.R. Tonks, D. Gaston, J.W. Peterson, D. Andrs, P.C. Millett, and B.S. Biner. A quantitative comparison between c0 and c1 elements for solving the cahn–hilliard equation. *J Comput Phys*, 236:74–80, 2013.
[84] Z. Zhang and Z. Qiao. An adaptive time-stepping strategy for the cahn-hilliard equation. *Commun Comput Phys*, 11:1261–1278, 2012.